NASA Technical Paper

3647

September 1996

Aeroservoelastic Modeling and Validation of a Thrust-Vectoring F/A-18 Aircraft

Martin J. Brenner

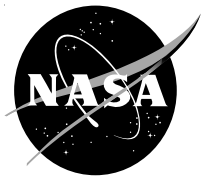

NASA Technical Paper 3647

1996

Aeroservoelastic Modeling and Validation of a Thrust-Vectoring F/A-18 Aircraft

Martin J. Brenner
Dryden Flight Research Center
Edwards, California

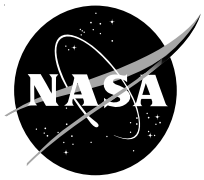

National Aeronautics and Space Administration

Office of Management

Scientific and Technical Information Program

CONTENTS

TABLES

FIGURES

ABSTRACT

An F/A-18 aircraft was modified to perform flight research at high angles of attack (AOA) using thrust vectoring and advanced control law concepts for agility and performance enhancement and to provide a testbed for the computational fluid dynamics community. Aeroservoelastic (ASE) characteristics had changed considerably from the baseline F/A-18 aircraft because of structural and flight control system amendments, so analyses and flight tests were performed to verify structural stability at high AOA. Detailed actuator models that consider the physical, electrical, and mechanical elements of actuation and its installation on the airframe were employed in the analysis to accurately model the coupled dynamics of the airframe, actuators, and control surfaces. This report describes the ASE modeling procedure, ground test validation, flight test clearance, and test data analysis for the reconfigured F/A-18 aircraft. Multivariable ASE stability margins are calculated from flight data and compared to analytical margins. Because this thrust-vectoring configuration uses exhaust vanes to vector the thrust, the modeling issues are nearly identical for modern multiaxis nozzle configurations. This report correlates analysis results with flight test data and makes observations concerning the application of the linear predictions to thrust-vectoring and high-AOA flight.

NOMENCLATURE

A/D	analog to digital
AOA	angle of attack, deg
ASE	aeroservoelastic
DFRC	Dryden Flight Research Center, Edwards, California
FEM	finite-element model
G	gravitational acceleration
GVT	ground vibration test
HARV	High Angle of Attack Research Vehicle
HOM	high-order actuator model
INS	inertial navigation system
KEAS	knots equivalent airspeed
LOM	low-order actuator model
m_0	surface mass
MDOF	multiple degrees of freedom
MIMO	multi-input–multi-output
N_y	lateral acceleration, Hz
NASA	National Aeronautics and Space Administration
OBES	onboard excitation system
p	roll rate, Hz
r	yaw rate, Hz
RFCS	research flight control system
RSRI	roll stick to rudder interconnect
s	Laplace variable
SDOF	single degree of freedom
SISO	single-input–single-output
STARS	structured and aeroservoelastic analysis routines
TVCS	thrust-vectoring control system

V	true velocity
ZOH	zero order hold
α	angle of attack, deg
β	angle of sideslip, deg
Δ	complex perturbation
δ	control-surface displacement
$\dot{\delta}$	control-surface rate
η_a	actuator state
η_e	flexible-mode state
η_r	rigid-body state
θ	pitch angle, deg
μ	multivariable stability margin
ϕ	roll angle, deg
ω	vibration frequency

INTRODUCTION

Agility, performance requirements, and quest for a better understanding of aerodynamics by computational fluid dynamicists have stimulated the aerospace community to earnestly pursue high-angle-of-attack (AOA) flight. Modern fighter aircraft are being built or reconfigured for enhanced controllability and maneuverability in stalled and poststalled flight regimes. The demanding flight control tasks at these conditions introduce some elements of uncertainty in the modeling of aircraft dynamics.

The aeroservoelastic (ASE) dynamics include the coupling of structural dynamics, control dynamics, sensing, aerodynamics, and actuation. Structural dynamics can be accurately, although laboriously, modeled and validated with ground test data. Because the primary errors in control feedback sensing come from airdata measurements, calibration is necessary to quantify the affects of these measurements on the integrity of the system and to make corrections so that feedback can also be reliably modeled. Aerodynamics and actuation are the remaining components of the modeling process.

Linear ASE predictions are suspect even at moderate AOA because they are based on linear assumptions of potential flow, elastic dynamics, and control dynamics. Vorticity and separation in the airflow violate the presumptions of the analysis. In addition, extreme static loads, asymmetric or random aerodynamic disturbances, nonlinear actuator dynamics, and unexpected coupling mechanisms are possible sources of deviation from predictions based on conventional unsteady aerodynamic and actuator modeling. Multirate control laws with digital notch filters require careful formulation of the sampled data system response and derivation of stability estimates. The extrapolation of linear methods at moderate and especially high AOA is empirical at best and should be verified with test data.

At many flight conditions, unsteady measured data are generally not available, and more precise modeling with computational fluid dynamics codes is not feasible for predicting aeroelastic phenomena. Engine thrust vectoring is a promising technology to compensate for the loss of aerodynamic control power but introduces another coupling mechanism in the form of propulsive forces that propagate through the fuselage where the feedback sensors are located. The engine exhaust plume states, which are difficult to determine for a variety of flight conditions, power levels, and exhaust conditions such as turning vane displacements, nozzle area, and unsteady flow, create a source of uncertainty.

ASE stability analyses at predominantly low AOA have been reported for advanced aircraft, such as the X-29A Advanced Technology Demonstrator (refs. 1 and 2) and F-15 STOL Maneuver Technology Demonstrator (ref. 3), but few published works have addressed ASE modeling issues for thrust-vectored configurations or high-AOA flight. The primary modeling issues are as follows:

1. Capability of the finite-element model (FEM) to capture primary structural dynamics, especially at feedback sensor locations
2. Fidelity of actuator modeling necessary to correlate with ground tests and for analysis at any flight condition
3. Discretization techniques for multirate control laws
4. Complexity of aerodynamic modeling necessary to capture critical dynamics related to structural stability
5. Effect of propulsive forces, buffet, separation, and other high-AOA aerodynamic uncertainties on predicted stability levels
6. Types of flight-derived stability estimates required for model validation at high AOA

The first four concerns apply to general flight regimes, and the last two apply to thrust-vectored and high-AOA regimes.

Correlation with closed-looped ground tests is traditionally achieved by modeling actuators with a linear spring attached to the structure and matched transfer function representations. High-AOA flight is predominantly performed at low dynamic pressures, so servoelastic dynamics is expected to dominate any unsteady aerodynamic effects on structural stability. Therefore, for more realistic predictions of actuation and associated coupling mechanisms, detailed actuator models, which consider the physical, electrical, and mechanical elements of actuation and its installation on the airframe, are employed to accurately analyze the coupled dynamics of the airframe, actuators, controller, and aerodynamics.

This report describes the ASE modeling procedure, ground test validation, flight test clearance, and test data analysis for the F-18 high-AOA research vehicle with thrust-vectoring control system (HARV TVCS). Open- and closed-loop ground tests were performed to validate the FEM for modal dynamics, tune sensor feedback functions and actuator models, and compare closed-loop responses between the aircraft and the hybrid analog discrete servoelastic model without aerodynamics. This report discusses the sensitivity of stability estimates to system discretization and aerodynamic modeling, compares analysis results with transfer functions derived from flight test data, and draws conclusions regarding the effectiveness of linear predictions for high-AOA flight.

AIRCRAFT DESCRIPTION, MODIFICATIONS, AND ASE CONCERNS

This section describes the F/A-18 HARV TVCS aircraft, including structural modifications and control system features, and discusses concerns about modeling uncertainties.

Structural Modifications

The F/A-18 HARV TVCS aircraft (fig. 1) is a modification of a preproduction twin jet engine fighter F-18 built by McDonnell Douglas Aerospace Corporation, (St. Louis, Missouri). The aircraft has clean fixed wings, wingtip folds for aircraft carrier storage, wingtip instrumentation pods augmented with airdata-sensing devices in place of missile launcher rails, outboard ailerons, inboard trailing-edge flaps, and inboard and outboard leading-edge flaps. All actuators have redundant hydroelectric servovalves and are dual tandem powered. The leading-edge flap is the only rotary mechanical system. Twin vertical tails angle outward 20° from the vertical, horizontal stabilators are attached to the aft fuselage, and leading-edge extensions are attached from each wing root junction along the fuselage to the canopy station.

EC91 0010-6

Figure 1. F/A-18 HARV TVCS aircraft in flight.

The F/A-18 HARV TVCS aircraft was modified at the National Aeronautics and Space Administration (NASA) Dryden Flight Research Center (DFRC) to perform flight research at high AOA by using thrust vectoring and control law concepts for agility and performance enhancement and to provide data for correlation with computational fluid dynamics solutions. Modifications include the addition of Inconel[1] (primarily a nickel alloy) vanes in each engine exhaust for thrust vectoring and corresponding ballast in the forward fuselage to maintain a center-of-gravity location; a research flight control system for feedback control of aerodynamic surfaces and the vanes; an inertial navigation system (INS) for AOA and sideslip rate feedback; wingtip AOA vanes and pressure probes (for airdata research purposes); and additional instrumentation for loads, vane temperatures, and structural dynamics. As a result, the HARV TVCS aircraft has significantly different systems and structural characteristics from the basic F/A-18 aircraft. Because of this reconfiguration ASE characteristics were expected to change considerably from the basic F/A-18 aircraft.

The TVCS structural modifications include a vectoring system with three engine exhaust vanes radially displaced about each engine nozzle. Figures 2 and 3 show the arrangement and dimensions of these vanes. During activation, only two of the three vanes on each engine are used to direct the thrust, and the idle vane is removed from the exhaust plume because of physical interference with the vectored plume. The horizontal stabilator was modified by trimming two percent of the trailing-edge inboard area to provide clearance for the aft end of the outboard vane fairing assembly.

The vane assembly added 1600 lb, and the corresponding ballast in the forward fuselage just in front of the cockpit amounted to 700 lb. An additional 900 lb was added with the installation of the spin chute and subsystem modifications, which included emergency batteries, modified radome, steel reinforcement, and wiring. Thus, the total weight increase from the basic aircraft is about 3200 lb. This increase resulted in an aft center-of-gravity shift of 4.4 in. for the empty aircraft. The internal fuel capacity is 10,620 lb, and full-takeoff gross weight is about 40,000 lb.

[1]Inconel® is a registered trademark of Huntington Alloy Products Div., International Nickel Co., Huntington, West Virginia.

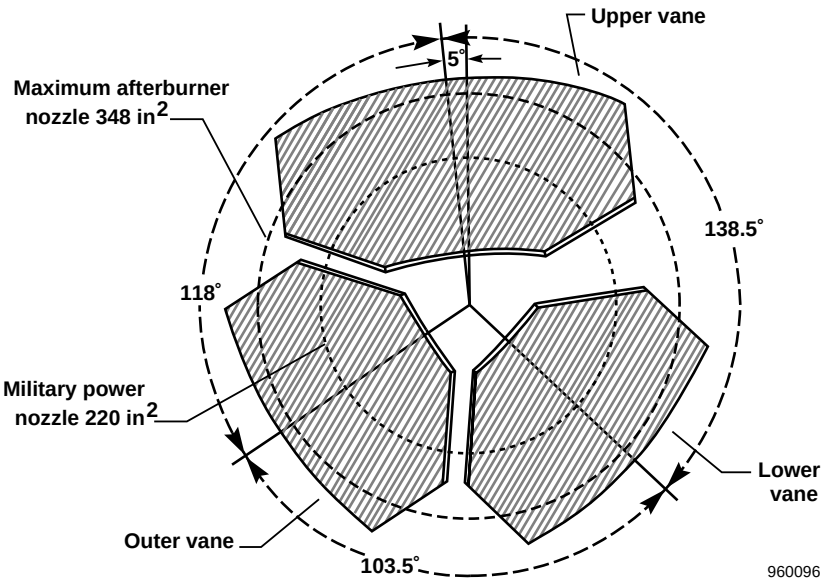

Figure 2. TVCS vane distribution for vanes fully extended into plume for left engine.

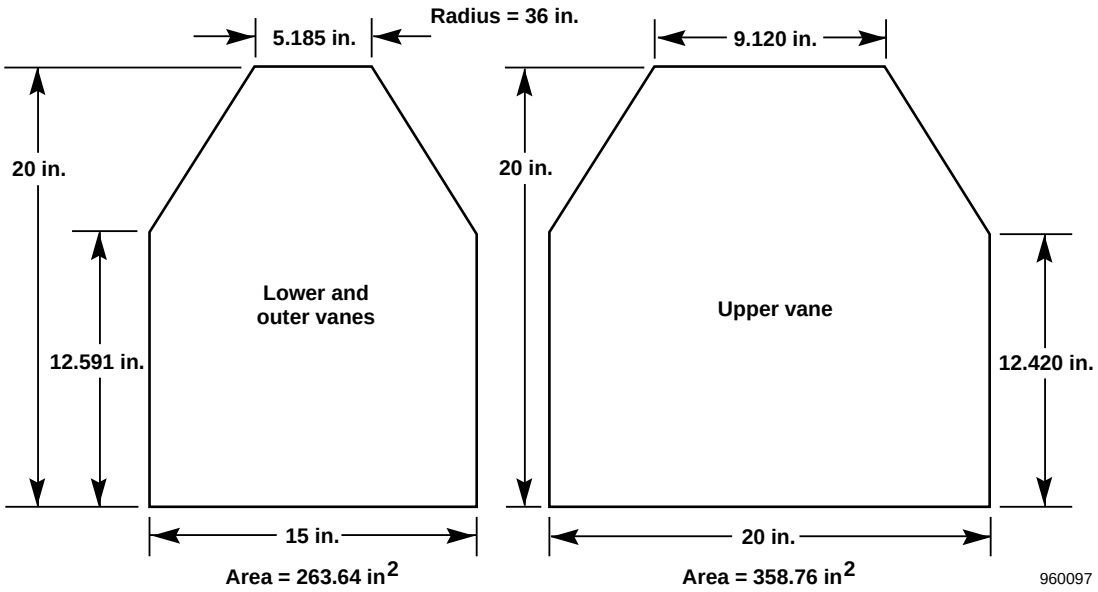

Figure 3. TVCS vane dimensions.

Flight Control Laws

Basic Flight Control System

McDonnell Douglas Aerospace designed the flight control laws for the basic and modified HARV TVCS F/A-18 aircraft. The F/A-18 basic controller was modified for the TVCS to permit communication with a research flight control system (RFCS) (ref. 4). The actuator commands from the RFCS are passed to the basic controller for redundancy checks before commanding actuation. Because the two control laws are computed concurrently, the

choice between the basic and RFCS control laws requires engaging the appropriate surface commands. Figures 4 and 5 display linearized versions of the basic feedback control laws (excluding stick and pedal paths) for longitudinal and lateral–directional control. In the longitudinal basic control laws, the horizontal stabilators react to normal acceleration, AOA from airdata vanes mounted on the nose, and pitch-rate feedback. Leading- and trailing-edge flaps respond to washed-out AOA as essentially trimming devices. Pitch rate is fed back at 80 Hz, but normal acceleration and AOA feedback are 40-Hz loops. All actuators are commanded at 80 Hz. Important features include proportional/integral feedforward followed by a 9.6-Hz digital notch filter for the fuselage first-bending mode.

Lateral–directional basic control uses roll rate (80 Hz), yaw rate (40 Hz), and lateral acceleration (40 Hz) to command differential stabilator, ailerons, leading-edge and trailing-edge flaps, and rudders at 80 Hz. A roll-to-yaw interconnect directs stabilator and aileron commands to the rudder through lead-lag compensation. Structural digital notch filters for fuselage and fin first-bending modes are 7 Hz and 17 Hz, respectively.

Research Flight Control System

The RFCS control laws were designed with independent techniques for longitudinal and lateral–directional axes (ref. 5). Both systems are multirate with INS computation delays over 75 msec for AOA and sideslip rate feedback. The logic used to convert a thrust-vector command to move the six vanes is a very complicated function of estimated gross thrust, throttle position, nozzle position, AOA, altitude, and other parameters (ref. 4). This function adds a 12.5-msec delay to the pitch and yaw jet commands.

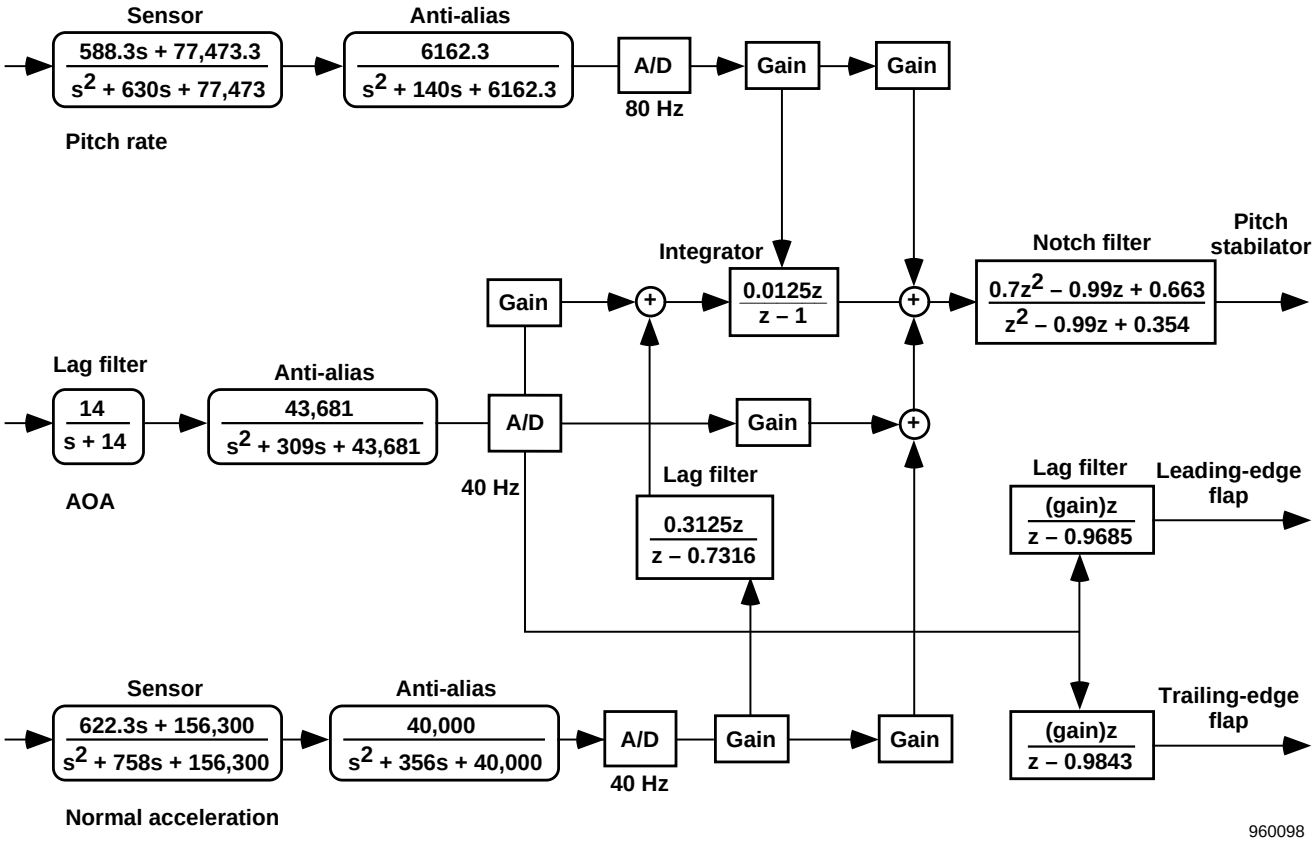

Figure 4. F/A-18 longitudinal basic control laws.

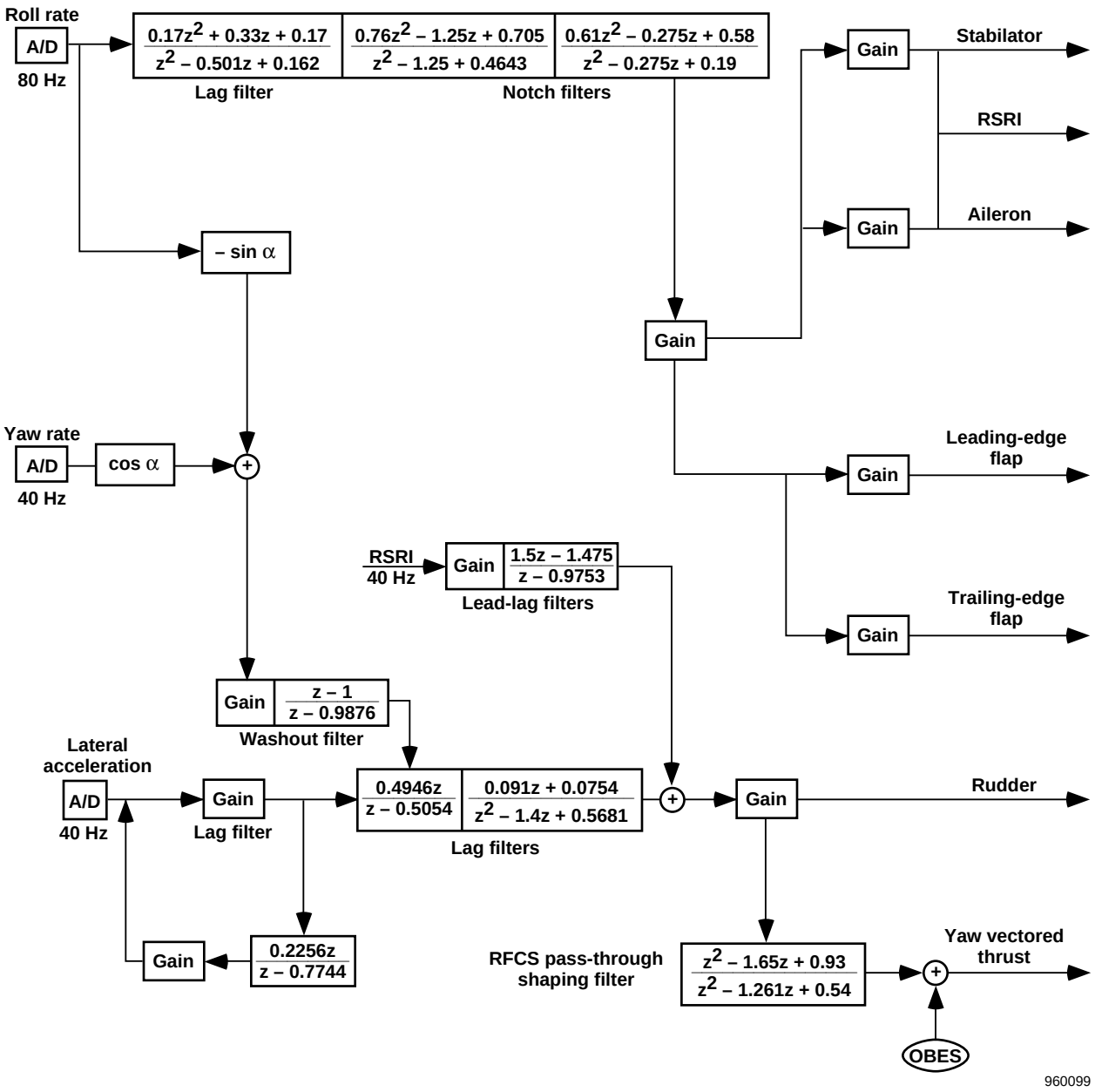

Figure 5. F/A-18 lateral–directional basic control laws with RFCS pass-through yaw-vectored-thrust command.

The INS derives AOA, sideslip angle, and rates from direction cosines, inertial velocity, rate gyros, and body axis accelerations. These control laws use standard shipset AOA vanes for angles less than 35° and INS-computed AOA at higher angles. Sideslip rate is INS computed at all flight conditions. The flight envelope varies from 15,000 to 35,000 ft altitude for all AOAs and a maximum Mach number of 0.7. Beyond an impact pressure of 150 lb/ft^2, the lateral–directional control laws are the basic control laws with an additional rudder command path to the yaw jet (fig. 5). RFCS control laws are called pass-through because they pass the rudder command to the yaw jet.

Longitudinal RFCS (fig. 6) commands symmetric stabilators, pitch-vectoring turning vanes, and leading- and trailing-edge flaps at 80 Hz to control pitch rate (sampled at 80 Hz) and AOA (sampled at 40 Hz). Structural filtering consists of a digital notch for the fuselage first-bending mode and is assisted by lag filters. At high AOA, the stabilator is the primary trimming surface. The turning vanes are used if the stabilator becomes ineffective for

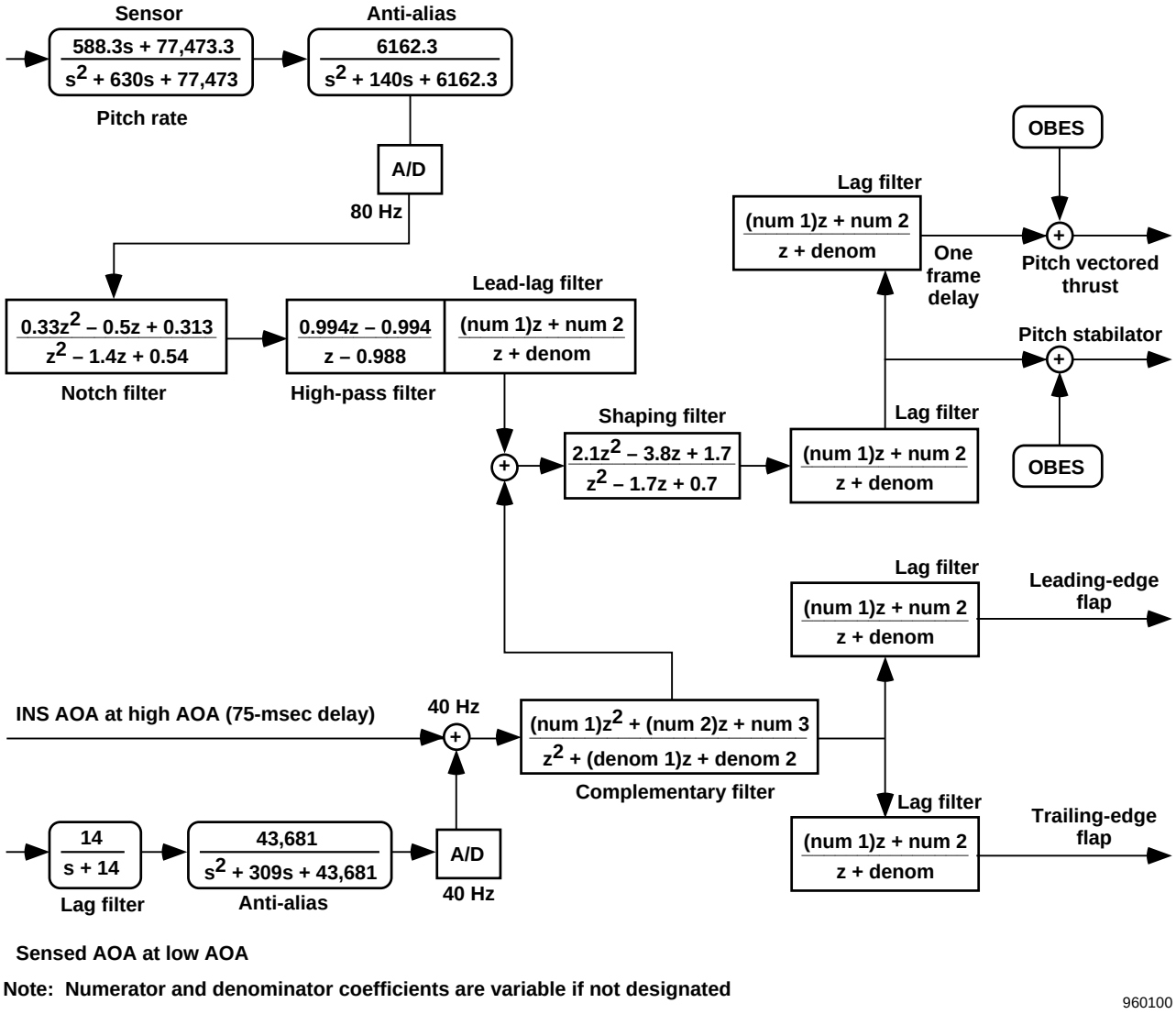

Figure 6. F/A-18 RFCS longitudinal control laws.

trimming. Proportional, integral, and other compensation is also implemented to get precise AOA control up to 70° for research flights and to obtain generally good high-AOA agility and maneuvering.

Lateral–directional RFCS (fig. 7) incorporates the INS sideslip rate (sampled at 40 Hz) as a feedback and commands all actuators at 80 Hz. The sideslip rate is calculated as

$$\beta = \frac{1}{V\cos(\beta)}\left(G * \cos(\theta) * \sin(\phi) + N_y\right) + p\sin(\alpha) - r * \cos(\alpha)$$

where V is true velocity, β is sideslip angle, θ is pitch angle, ϕ is roll angle, α is AOA, G is gravitational acceleration, p is roll rate, r is yaw rate, and N_y is lateral acceleration. The notch filters for fuselage first bending and fin first bending, and the lag filter from the basic control laws remain in the roll control loop. Lateral acceleration and sideslip rate are notch filtered for wing first bending. At high AOA, these forms of feedback enhance departure resistance, but at low AOA, only roll-rate feedback is used. Flaps are not employed as dynamic control mechanisms.

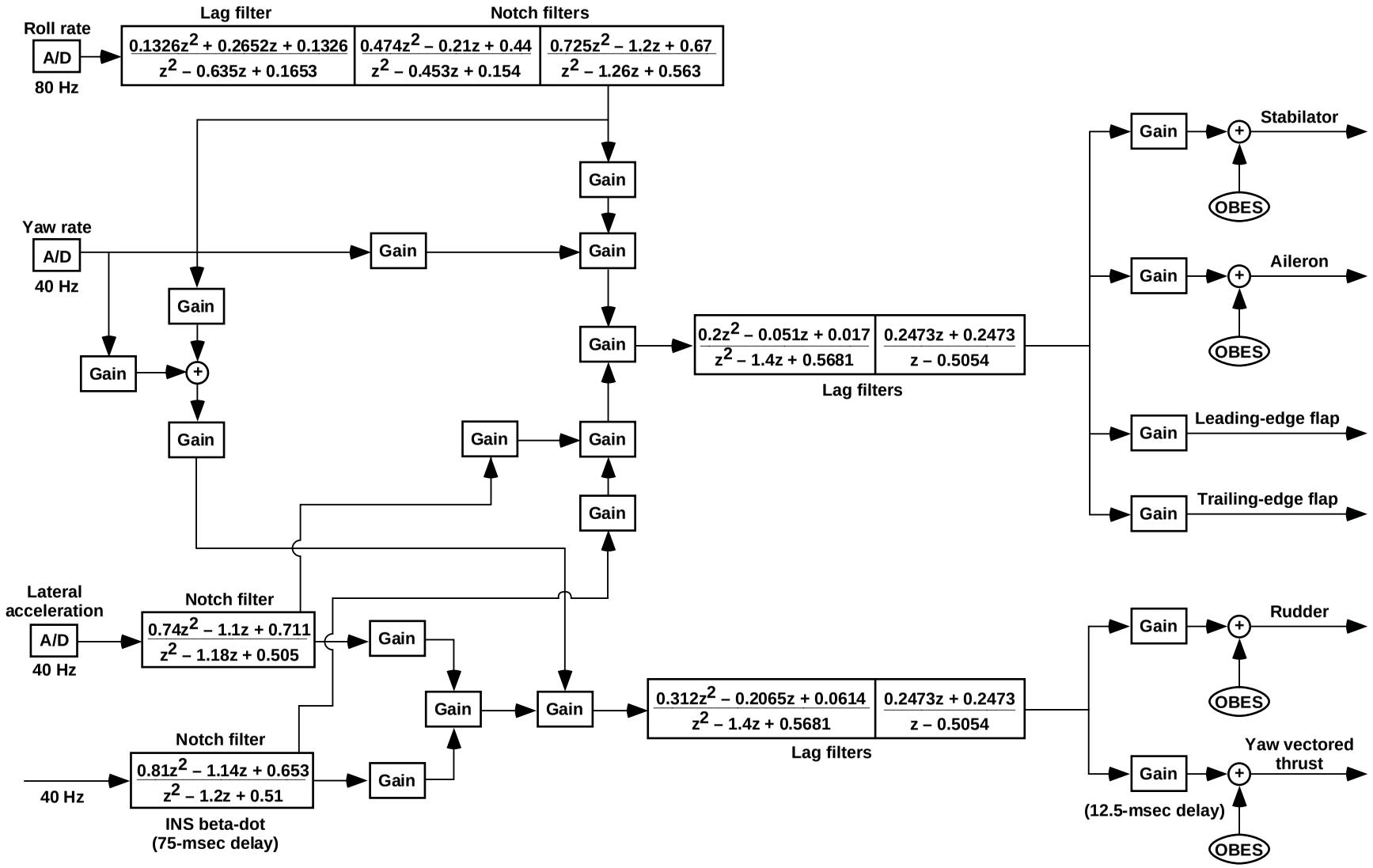

Figure 7. F/A-18 RFCS lateral–directional control laws.

Areas of Concern

Experience with the research X-29 aircraft demonstrates a very good correlation between linear ASE results and flight test results (ref. 1) at low AOA. Other test results (fig. 8) indicate that discrepancies are clearly evident at higher AOA. The AOA varies from 10° to 45°, corresponding to a Mach number range of approximately 0.7 to 0.3. The

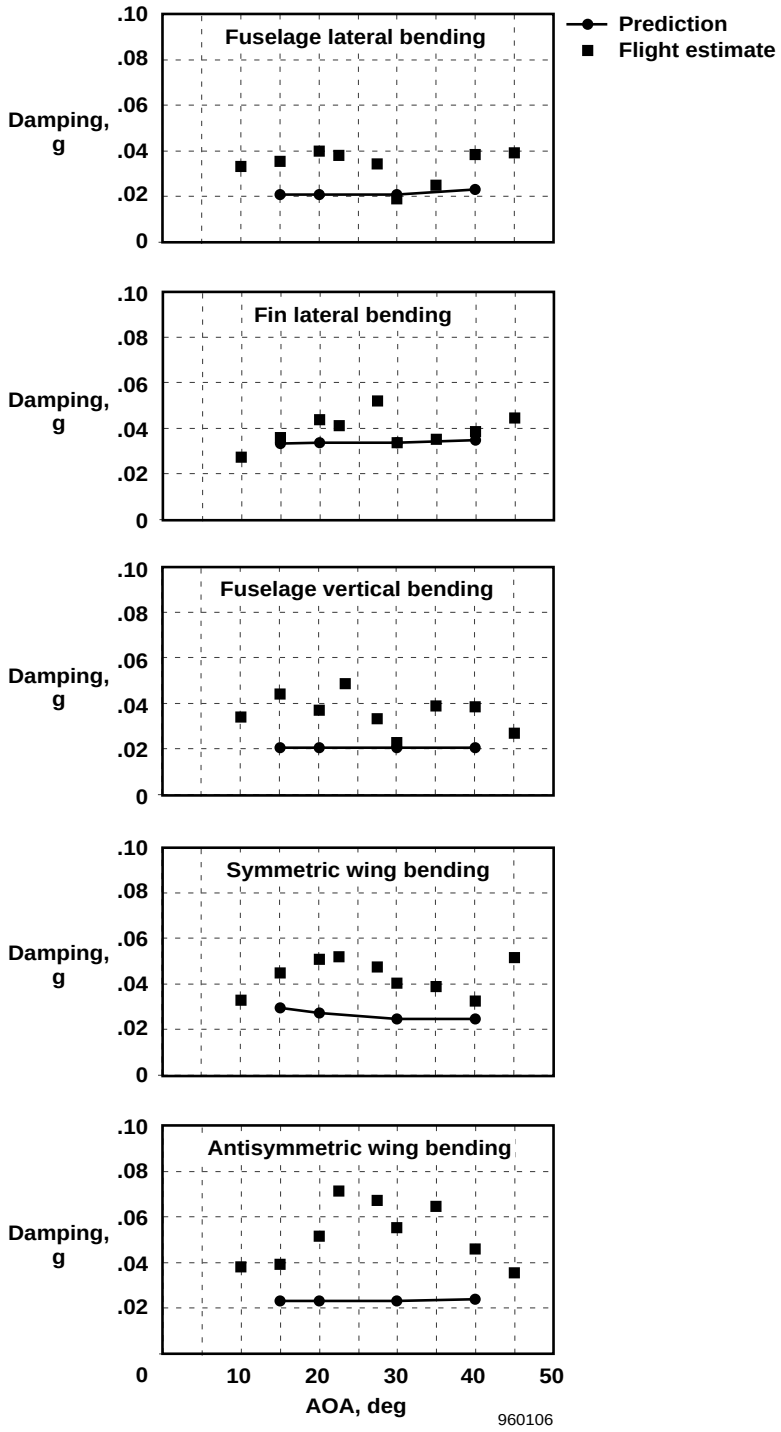

Figure 8. X-29 modal damping results at high AOA.

plots show that the first fuselage and fin bending mode damping trends are well predicted as a function of AOA but that both first wing-bending mode predictions disagree with flight damping estimates at moderate AOA. The sources of error were not investigated because predictions were conservative relative to the test results; however, the results cannot necessarily be generalized to other configurations. Errors may be attributed to vortical flow, buffet loads, flow separation, noisy data, or modal estimation technique.

Additional uncertainties include vane flutter and the effect of unknown nozzle and plume states on control system behavior. A novel type of ASE phenomenon exists from the high-temperature unsteady plume that emanates from the exhaust and the vane assembly attached to the fuselage. Coupling is suspect between the plume aerodynamics, vane structure, and actuation connecting the vanes to the fuselage. Furthermore, the engine throttle is not the same at all conditions, and the vane configuration varies dramatically as a function of flight condition and maneuver. Whether such uncertainties are significant for stability is a matter of concern because only a simplified analysis was feasible.

Because of this uncertainty and other possible sources of modeling error for the HARV TVCS aircraft, extensive ground tests were executed for model validation and robust stability was inspected for the basic and RFCS control laws. Because modeling and analysis procedures are essentially the same for both control laws, the basic analysis is not discussed in this report except to state that the entire subsonic envelope, up to Mach number 0.9, was cleared from predictions and flight test. Three test points were chosen as critical flight conditions, and modal frequency and damping estimates from test data compared favorably with predictions (table 1) for the primary modes of interest.

Table 1. F/A-18 HARV TVCS basic control system stability results for primary modes.

Flight condition (Mach/ Altitude)	Symmetric modes				Antisymmetric modes					
	First wing		First fuselage		First wing		First fuselage		Wing torsion	
	g-damping	Frequency, (Hz)	*g*-damping	Frequency, (Hz)	*g*-damping	Frequency, (Hz)	*g*-damping	Frequency, (Hz)	*g*-damping	Frequency, (Hz)
M 0.6/15 kft										
Predicted	0.11	5.9	0.029	7.8	0.050	9.1	0.022	7.1	0.036	12.7
Measured	0.08	5.8	0.031	8.1	0.036	8.9	0.019	7.6	0.025	12.6
M 0.7/15 kft										
Predicted	0.13	5.9	0.031	7.8	0.054	9.1	0.023	7.1	0.038	12.7
Measured	0.14	6.0	0.040	8.4	0.053	9.8	0.021	7.1	0.019	12.3
M 0.6/10 kft										
Predicted	0.15	5.9	0.033	7.8	0.063	9.0	0.023	7.1	0.042	12.7
Measured	0.11	6.2	0.035	8.4	0.043	8.9	0.017	7.6	0.025	12.8

AEROSERVOELASTIC MODELING PROCEDURE

The ASE modeling procedure presented in this section covers the details and integration of aerodynamics as well as structural and actuator dynamics. Modal analysis and flutter predictions are also tabulated.

Finite-Element Modeling

The quality of a flutter or ASE analysis depends predominantly upon the detail of the FEM. Representing complicated structures with a large number of elements improves the accuracy but also increases the complexity of

the FEM. Optimization of the number of nodes and elements to attain sufficient accuracy may be computationally prohibitive, so it is vital that the model design emphasizes critical areas but maintains a minimum number of elements. When structural modifications are necessary, the critical areas may need to be adjusted and the model may require reexamination for completeness and numerical accuracy.

An intensive normal mode analysis using the structured and aeroservoelastic analysis routines (STARS) computer code (ref. 6) proved vital for validating the FEM modal dynamics against measured data. The TVCS modifications required substantial additions to the baseline F/A-18 aircraft. The TVCS comprises fairing assemblies, bell cranks, vanes, and hydraulic actuators. Beam elements, rigid bars, and quadrilateral plates (fig. 9) were used to model the modifications, and the entire aircraft model yielded 260 nodes and 340 elements. Free-vibration structural analyses for the half-aircraft symmetric and antisymmetric boundary conditions were computed to generate modal frequencies, generalized masses, and mode shapes, which were then used to guide the ground vibration test (GVT) procedure. Table 2 compares computed modal frequencies with GVT results to show the excellent correlation for primary symmetric and antisymmetric modes.

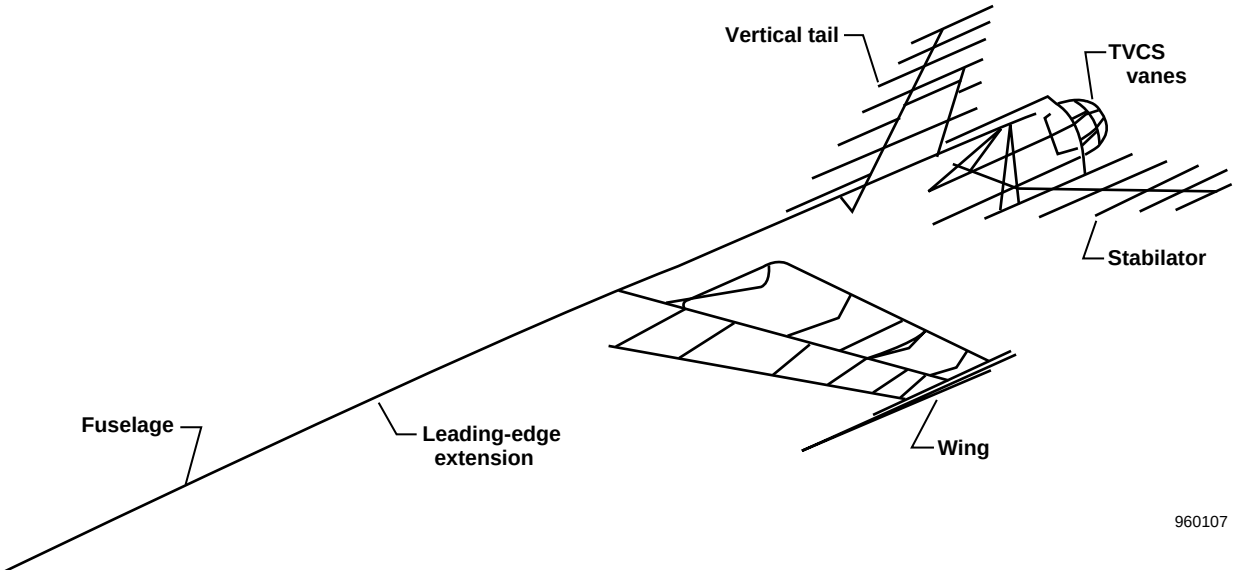

Figure 9. F/A-18 HARV TVCS FEM.

Aerodynamic Modeling

Subsonic linear unsteady aerodynamic forces were calculated using the doublet lattice method (ref. 7) for flutter analysis and ASE models. Aerodynamic paneling is used to compute the unsteady aerodynamic forces for purely oscillatory motion of each mode for a range of specified reduced-frequency values. These generalized aerodynamic forces are tabulated complex values which are valid only for undamped oscillatory motion. These values are extended to the Laplace domain using approximate analytic continuation to represent aerodynamic damping. Reference 8 outlines some methods to approximate the generalized force coefficients with matrix formulations of rational functions in s, the Laplace variable. These methods, referred to as Padé approximates in the reduced frequency domain, are estimates of the time lags associated with unsteadiness in the flow. The reduced frequency, or Strouhal number, which is defined as the ratio of the velocity of vibration to the velocity of the air, is expressed as $\omega\bar{c}/2V$, for vibration frequency ω, true velocity V, and characteristic length of the half chord $\bar{c}/2$. Subsequently, a linear time invariant state-space realization can be formulated for each flight condition.

Table 2. Free vibration analysis results for F/A-18 aircraft.

Symmetric modes.		
Primary motion	Predicted (frequency, Hz)	GVT (frequency, Hz)
Lightweight (2500 lb fuel)		
Wing first bending (W1B)	5.83	6.08
Fuselage first bending (F1B)	7.97	8.19
Wing first torsion (W1T)	11.71	11.78
Stab first bending (S1B)	13.77	13.78
Fin first bending (Fin 1B)	15.92	15.72
Fuselage second bending (F2B)	16.39	16.20
Wing second bending (W2B)	18.05	---
Wing fore-aft (WFA)	18.86	---
Vane rotation	22.1	20.1
Inboard flap rotation (IFR)	23.70	---
Wingtip torsion (WTT)	27.52	---
Heavy weight (full fuel)		
Wing first bending (W1B)	5.75	6.02
Fuselage first bending (F1B)	7.45	7.76
Wing first torsion (W1T)	11.64	11.80
Stab first bending (S1B)	13.68	13.63
Fin first bending (Fin 1B)	15.92	15.68
Fuselage second bending (F2B)	15.34	15.23
Wing second bending (W2B)	17.05	17.01
Wing fore-aft (WFA)	18.19	---
Vane rotation	22.1	20.1
Inboard flap rotation (IFR)	23.50	---
Wingtip torsion (WTT)	27.47	---
Antisymmetric modes.		
Lightweight (2500 lb fuel)		
Fuselage first bending (F1B)	7.40	7.25
Wing first bending (W1B)	8.88	8.48
Wing first torsion (W1T)	12.03	12.20
Stab first bending (S1B)	13.69	13.58
Wing fore-aft (WFA)	15.36	15.25

Table 2. Concluded.

Antisymmetric modes.		
Primary motion	Predicted (frequency, Hz)	GVT (frequency, Hz)
Lightweight (2500 lb fuel)		
Fin first bending (Fin 1B)	15.85	---
Fuselage first torsion (F1T)	19.50	---
Fuselage second bending (F2B)	21.83	---
Vane rotation	22.1	20.1
Inboard flap rotation (IFR)	23.33	---
Fore-fuselage torsion (FTT)	24.36	---
Heavy weight (full fuel)		
Fuselage first bending (F1B)	6.86	6.64
Wing first bending (W1B)	8.61	8.33
Wing first torsion (W1T)	12.02	12.13
Stab first bending (S1B)	13.57	13.45
Wing fore-aft (WFA)	14.99	15.09
Fin first bending (Fin 1B)	15.56	15.31
Fuselage first torsion (F1T)	18.76	22.00
Fuselage second bending (F2B)	21.01	---
Vane rotation	22.1	20.1
Inboard flap rotation (IFR)	23.02	---
Fore-fuselage torsion (FTT)	23.98	---

Justification for the application of forced-oscillation linear theory is based on the following assumptions from references 9 and 10:

- The structural vibrations about a fixed-mean AOA are relatively small, so the relation between system displacements and motion-dependent structural and aerodynamic forces is linear.
- Small-amplitude oscillatory motion has little influence on the unsteady pressures resulting from flow separation.

In addition, for fully separated flow above 30° AOA, it is assumed that:

- Aerodynamic forces due to modal vibration do not change appreciably as a function of AOA because the pressures remain essentially constant chordwise for a fixed-mean AOA.
- At low dynamic pressure where sustained high-AOA flight is commonly performed, unsteady airloads due to modal vibration are small and can be reasonably estimated with potential theory.

In this study, the method of least squares detailed in reference 1 was used to approximate a Padé partial fraction approximation to the unsteady aerodynamic forces as a function of reduced frequency. The number of partial

fractions used to fit the doublet-lattice data is the order of the fit. Padé fits to the doublet-lattice aerodynamics were designated as fourth order for flutter calculations and zero order for later ASE analyses. From a computational point of view, low-order ASE models are preferred because they reduce the cost of stability analyses. Several stability analyses must be performed at each flight condition, and the computational cost increases dramatically with the order of the system. Because the actuator models add a considerable number of states, the lowest order aerodynamic model with adequate accuracy is desired. First, steady aerodynamic data from a linearized version of the full-aircraft simulation database were incorporated into the generalized aerodynamic stiffness and damping matrices (ref. 1), thereby imposing the constraint that the aerodynamic forces near zero-reduced frequency match the wind-tunnel based measured data. Then, the low-order model simply represented the unsteady aerodynamics as a residual static correction to the steady aerodynamic data, and no aerodynamic states were added. Alternatively, a high-order model can add up to four states for each mode (ref. 8), which makes the analysis computationally very expensive.

Because of the complexity of scheduling individual vane displacements to achieve a commanded vectored thrust direction, the vanes were combined to derive a vectored thrust control mode with respect to a specified thrust level. Vectored thrust force effectiveness was reduced to the steady component of the plume dynamics acting on the vane configuration that was used to derive the mode shape. The orientation of each vane determined the force transmission to the aircraft through the attachment structure. These force effectiveness data were obtained from tests as described in reference 11. Unsteady plume effects on the vanes were not modeled.

The assumption is that on the average, all vanes have the same loading as a function of flight condition. Because the control system attempts to idle one vane in each plume at all times to avoid interaction with the desired thrust vector, this assumption is considered reasonable because, at any flight condition, each vane will travel between limits of idle and a deflection necessary to achieve a vectored thrust direction. While one vane in each plume is idling, the other two must compensate to maintain a commanded thrust-vector angle. There is no reason to expect that any one vane is a dominant load-carrying member when compared to the others in a steady-state maneuver.

For current and future configurations using multiaxis thrust vectoring with moving nozzles, the modeling issues are very similar to an external vane configuration except that the vanes of the nozzle are internally attached to the structure through the actuation mechanism. For instance, coupling will be of a different nature, but loading on the nozzles will still be somewhat concentric with approximately the same bandwidth as the TVCS. The major distinction will be the details of the attachment structure from the vane actuation to the fuselage. External aerodynamics on the nozzles can be ignored, and the plume will be even more constrained in the internal arrangement so that modeling uncertainties caused by plume dynamics are expected to be less significant. Because this formally makes little difference, the analysis of the external vane configuration can be generalized to any production thrust-vectoring mechanism.

Table 3 compares flutter speeds for the HARV TVCS aircraft from the aeroelastic state A-matrix (ref. 1) to those for the basic F/A-18 aircraft solutions. A sea-level condition at Mach 0.9 where $g = 0.02$ structural damping is used for the flutter results because the flight envelope is limited to subsonic. The ASE A-matrix contains all augmented

Table 3. F/A-18 flutter results.

	Symmetric		Antisymmetric	
Aircraft	Velocity, KEAS	Frequency, Hz	Velocity, KEAS	Frequency, Hz
Light weight (2500 lb fuel):				
Basic F/A-18	759.9	7.39	857.1	10.08
HARV TVCS	739.1	8.08	783.7	9.51
Heavy weight (full fuel):				
Basic F/A-18	770.8	7.30	871.3	9.93
HARV TVCS	701.4	7.73	765.8	9.35

aerostructural dynamics. The modes with the lowest flutter speeds are shown to be symmetric fuselage first bending at about 8 Hz and antisymmetric first wing bending at about 10 Hz. The lowest computed flutter speed, 701.4 kn equivalent airspeed (KEAS) for the symmetric mode, corresponds to Mach number 1.06 at sea level and Mach number 1.4 at an altitude of 15,000 ft. Modifications from the basic F/A-18 aircraft to the HARV TVCS aircraft resulted in decreased flutter speeds that were still well outside the desired flight envelope.

Actuator Modeling

The validity of an ASE model depends on not only the dynamic modeling of its components but also the coupling between these components. The airframe, aerodynamics, actuation, and the control system must be modeled accurately over a desirable and consistent frequency range. Actuator responses are customarily represented with transfer functions matched to test results, and control-surface stiffness with respect to the airframe is often modeled as a linear spring in the formulation of the airframe dynamics (ref. 12). More realistic predictions of airframe and actuation coupling that are consistent with advances in airframe and control-system modeling can be achieved by considering the physical properties of the system and its installation on the airframe. Detailed models, based on electrical, hydraulic, and mechanical characteristics with complex impedance effects, are required for more accuracy. Furthermore, at high-AOA and low-dynamic-pressure flight conditions, it is expected that unsteady aerodynamic forces will be less significant and hinge moments will be prominent (ref. 13).

The model described in Appendix A and represented in figure 10 is tuned to match measured results for each actuator. Discounting the states caused by structural and control-surface inertias, which are augmented as described

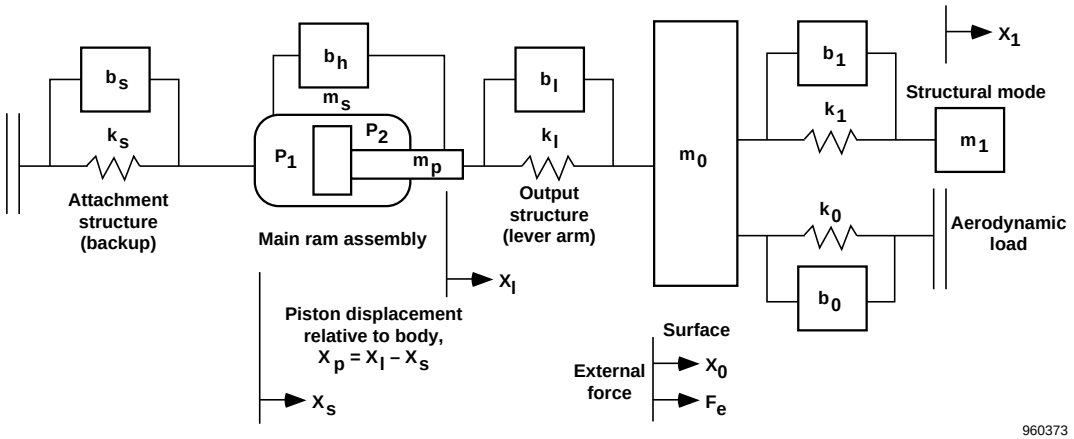

(a) Installation.

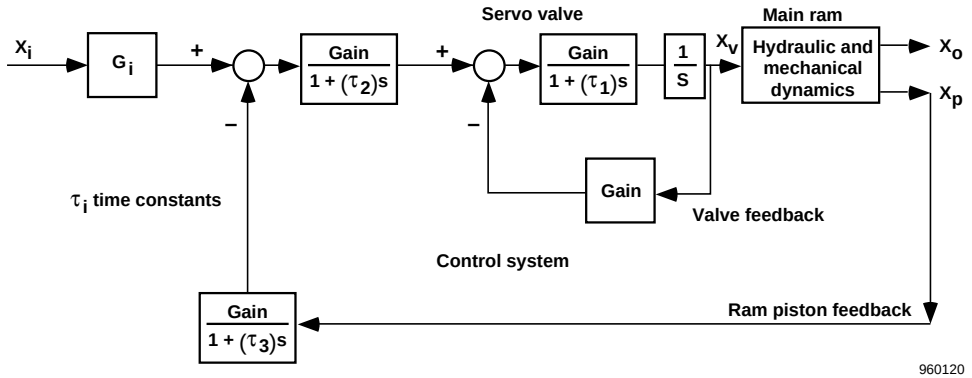

(b) Control system.

Figure 10. Sample actuator installation and control system.

in the next section, the high-order actuator models (table 4) for the F/A-18 HARV TVCS become seventh order for the aileron and vanes, tenth order for the stabilator, sixth order for the rudder, seventh order for the leading-edge flap, and eighth order for the trailing-edge flap, thereby adding 45 states for each symmetric set and antisymmetric set of structural modes. The differences in the number of states between actuators are predominantly determined by the type of servovalve and the inner loop servovalve feedback mechanism.

Table 4. High-order actuator model data.

Control surface	Transfer function
Trailing-edge flaps	$(1.5\times10^{14})\dfrac{(s+284)(s+808)}{(s+15.4)(s+76.2)(s+469)(s+1033)[s^2+2(0.98)(304)s+304^2][s^2+2(0.011)(817)s+817^2]}$
Ailerons	$(2.0\times10^{16})\dfrac{(s+356)}{[s^2+2(0.62)(69.1)s+69.1^2][s^2+2(0.94)(392)s+392^2][s^2+2(0.82)(746)s+746^2](s+17326)}$
Stabilators	$(3.0\times10^{14})\dfrac{(s+284)(s+808)[s^2+2(0.07)(72)s+72^2]}{(s+384)(s+1098)[s^2+2(0.6)(30)s+30^2][s^2+2(0.8)(127)s+127^2][s^2+2(0.9)(335)s+335^2][s^2+2(0.02)(718)s+718^2]}$
Rudders	$(2.6\times10^{13})\dfrac{(s+357)}{(s+14.4)(s+224)(s+431)(s+607)[s^2+2(0.006)(3335)s+3335^2]}$
Vanes	$(1.6\times10^{15})\dfrac{(s+356)}{(s+725)[s^2+2(0.79)(75)s+75^2][s^2+2(0.79)(475)s+475^2][s^2+2(0.82)(781)s+781^2]}$

State-Space Formulation

A detailed exposition of the procedure to augment the structural dynamics, aerodynamics, and sensor dynamics for an ASE analysis is given in reference 1. The structural model includes rigid-body, flexible, and control-surface modal dynamics as well as cross inertias. Steady aerodynamic forces from a linear panel method are replaced with those based on wind tunnel or other measured data before approximating the generalized aerodynamic forces for state-space representation. If stiffness effects from the control-surface rotation modes are computed from the FEM, representing the stiffness of the control surface against its actuator unit and supporting structure, they are discarded because they are replaced by the more accurate actuator model (fig. 10). In essence, the state equations take the following form for rigid-body states η_r, flexible-mode states η_e, control-surface displacements δ, and control-surface rates $\dot{\delta}$

$$\begin{pmatrix} \dot{\eta}_r \\ \dot{\eta}_e \\ \ddot{\eta}_r \\ \ddot{\eta}_e \end{pmatrix} = [A] \begin{pmatrix} \eta_r \\ \eta_e \\ \dot{\eta}_r \\ \dot{\eta}_e \end{pmatrix} + [B\acute{B}] \begin{pmatrix} \delta \\ \dot{\delta} \end{pmatrix}$$

$$y = [C] \begin{pmatrix} \eta_r \\ \eta_e \\ \dot{\eta}_r \\ \dot{\eta}_e \end{pmatrix} + [D\acute{D}] \begin{pmatrix} \delta \\ \dot{\delta} \end{pmatrix}$$

Actuator states are augmented by adjusting this matrix quadruple as

$$\begin{pmatrix} \dot{\eta}_r \\ \dot{\eta}_e \\ \ddot{\eta}_r \\ \ddot{\eta}_e \\ \hline \dot{\delta} \end{pmatrix} = \left[\begin{array}{cc} A & B \\ 0 & 0 \end{array}\right] \begin{pmatrix} \eta_r \\ \eta_e \\ \dot{\eta}_r \\ \dot{\eta}_e \\ \hline \delta \end{pmatrix} + \begin{bmatrix} \acute{B} \\ I \end{bmatrix} (\dot{\delta})$$

$$y = \begin{bmatrix} C & D \end{bmatrix} \begin{pmatrix} \eta_r \\ \eta_e \\ \dot{\eta}_r \\ \dot{\eta}_e \\ \hline \delta \end{pmatrix} + \begin{bmatrix} \acute{D} \end{bmatrix} (\dot{\delta})$$

The equation for control-surface rate $\dot{\delta}$ derived above (without the structural mode states x_1 and $\dot{x}_1$ since they are already included in η_e and $\dot{\eta}_e$ with the appropriate stiffness, damping, and inertial coupling terms) is augmented to this model for each actuator to produce

$$\dot{x} = \bar{A}x + \bar{B}\delta_d$$

$$y = \bar{C}x + \bar{D}\delta_d$$

where $x = [\eta_a \ \eta_r \ \eta_e \ \dot{\eta}_r \ \dot{\eta}_e \ \delta]$ includes all actuator states η_a. This aircraft plant description is augmented with control-system dynamics to construct the entire aircraft model.

AEROSERVOELASTIC ANALYSIS AND GROUND TEST RESULTS

Open-Loop Analysis and Ground Test

Low-order actuator models conventionally used for ASE analysis are typically second to fourth order, with a corresponding frequency used to define the dynamic stiffness between the airframe and control surface. These models are generated by simply fitting a low-order equivalent transfer function to measured data, with no regard for actuator details. Compliance with the structure is provided by the stiffness frequency, defined as $\omega = \sqrt{k_T/m_0}$, which is derived from a measured dynamic stiffness k_T and surface mass m_0. The transfer functions and stiffness frequencies used to generate the low-order actuator models in the current study are listed in table 5. (The

Table 5. Low-order actuator model data.

Control surface	Transfer function	Stiffness frequency, Hz
Trailing-edge flaps	$\frac{35^2}{s^2 + 2(0.71)(35)s + 35^2}$	4
Ailerons	$\frac{75^2}{s^2 + 2(0.59)(75)s + 75^2}$	16
Stabilators	$\frac{30.8^2}{s^2 + 2(0.51)(30.8)s + 30.8^2}$	2.4
Rudders	$\frac{72^2}{s^2 + 2(0.69)(72)s + 72^2}$	44
Vanes	$\frac{75^2}{s^2 + 2(0.59)(75)s + 75^2}$	8

leading-edge flap is not shown because of its relative insignificance in control authority.) Comparison plots and measured test results between the analytical high- and low-order models, are shown in figure 11 for the aileron actuator. This model is also representative of the other actuators. The low-order model was developed by matching a transfer function to the test data, and the high-order model was tuned to the data.

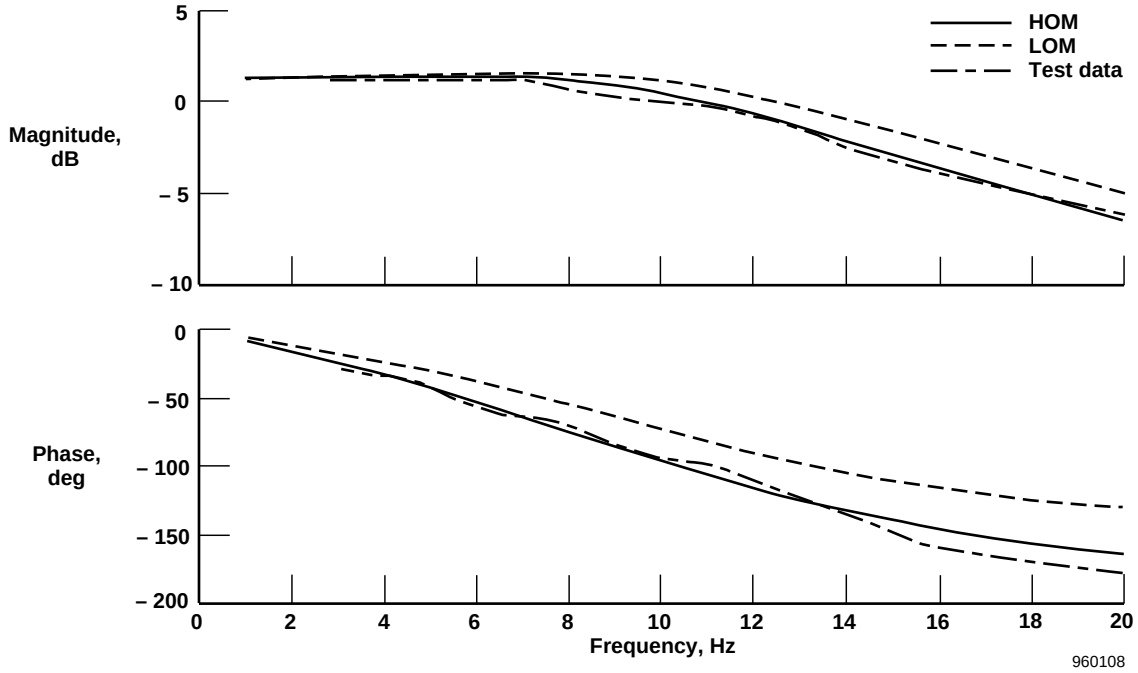

Figure 11. Frequency response of aileron high-order actuator model (HOM) and low-order actuator model (LOM) compared with test data.

GVTs provided sensor location dynamics from each mode relative to a shaker input or some other reference location. A reference location (input) was chosen on the aircraft for each vibrated mode, and the response (output) at the locations of the feedback sensors was measured to provide a relation for each mode between input at the reference and output at the sensor location. Normal acceleration, lateral acceleration, and pitch, roll, and yaw rate feedback were measured. These data were then incorporated into the analysis, assuming that the analytical mode shapes were correct to within a scale factor (i.e., the sensor location movement relative to the reference input could simply be multiplied by a constant factor).

Open-loop tests provide a better definition of control-system feedback than an interpolated FEM will produce. Figure 12 (heavy-weight aircraft) and figure 13 (lightweight aircraft) compare open-loop responses from stabilator to feedback locations for FEM-derived interpolated sensor motions and those corrected with measured GVT data. Clearly, the differences can be serious enough to require that the measured responses be used in the analyses.

Modal dynamics at the sensor locations are input to the usual linear sensor models used for control-system analysis. RFCS control laws resort to shipset AOAs for angles less than 35° and INS AOAs at higher angles. The INS sideslip rate is fed back throughout the envelope. However, AOA and INS feedback are not realizable from a ground test. Sideslip rate and AOA, therefore, are approximated by the dynamics of their respective generalized rigid-body modes (ref. 14) at the center of mass in the body-fixed reference axes. This is the inertial position of the origin of the body axes, or the instantaneous center of mass of the aircraft.

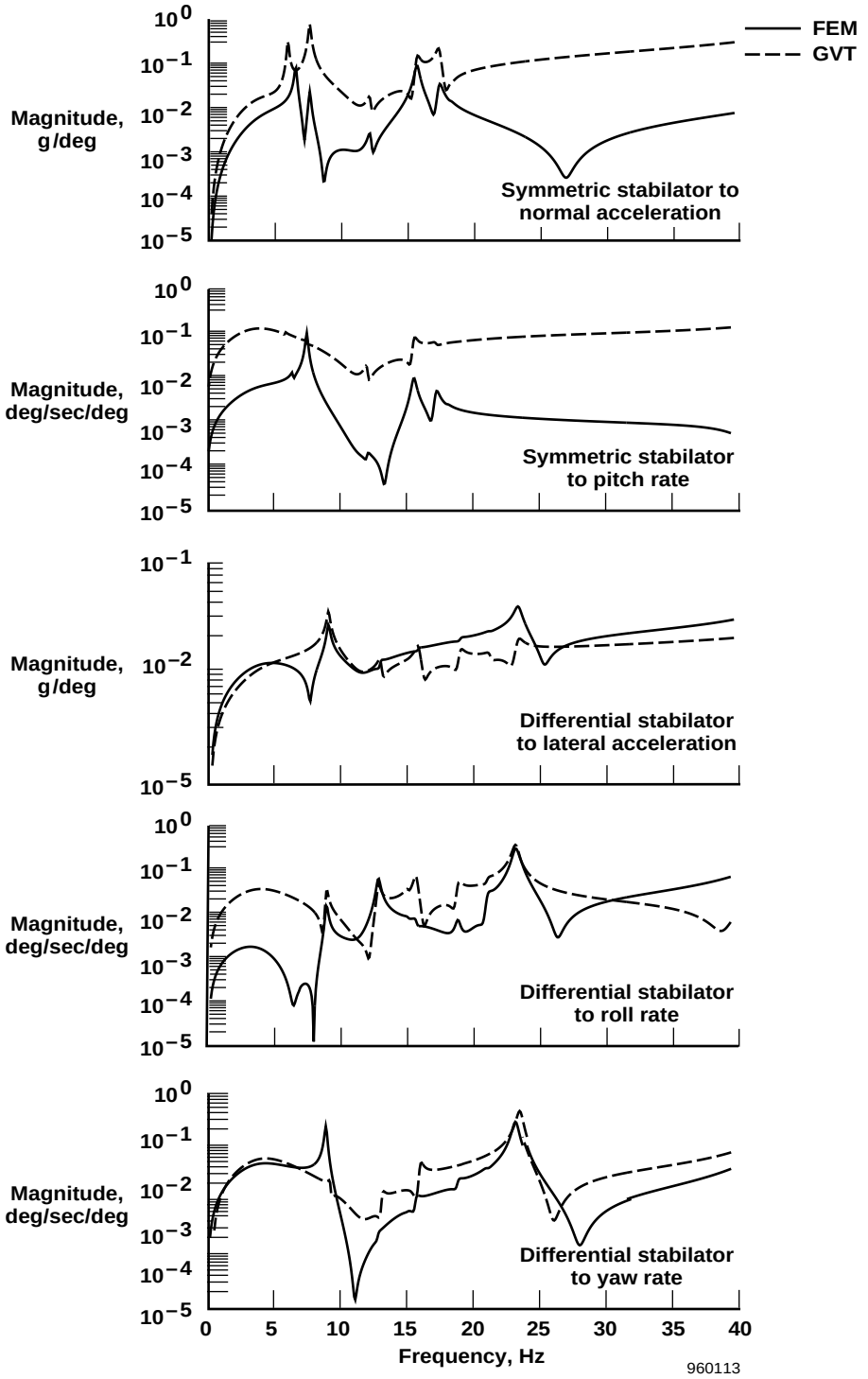

Figure 12. Comparison between FEM-interpolated and GVT-derived heavy-weight aircraft open-loop responses from horizontal stabilator to selected feedback locations.

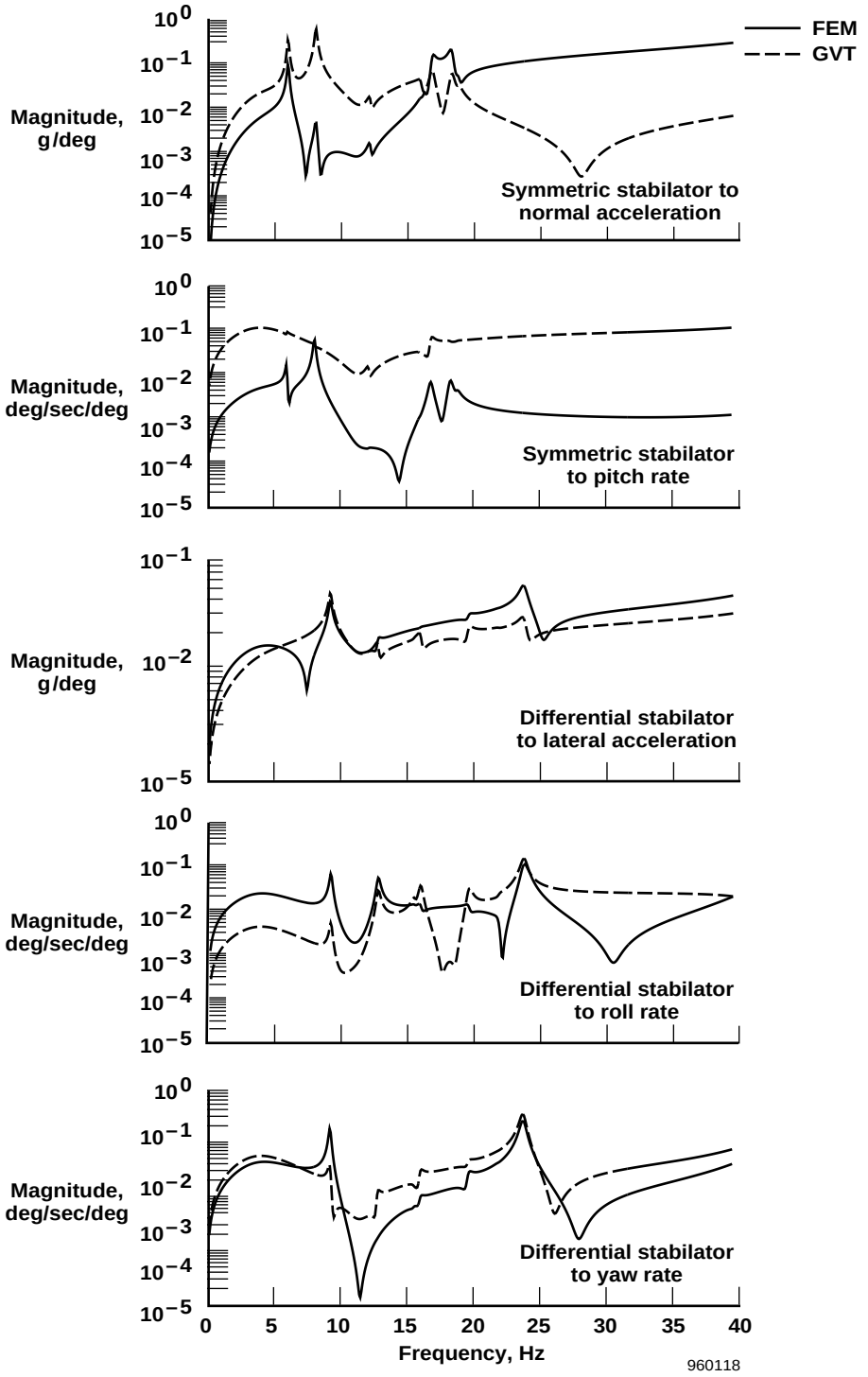

Figure 13. Comparison between FEM-interpolated and GVT-derived lightweight aircraft open-loop responses from horizontal stabilator to selected feedback locations.

Closed-Loop Modeling, Ground Test, and Analysis Results

Controls Augmentation

Modeling the dynamics of controller analog elements is well understood and proceeds in the usual manner for ASE modeling. Modeling the frequency content of continuous signals with linear analog elements is as precise as the premise of linearity and presents no difficulty when augmenting the control-system dynamics with the plant quadruple. The resulting augmented system is a linear description of the coupled interaction between controller and plant, which is as accurate as the assumptions that went into the modeling process. Modern controllers, however, are discrete implementations and often structured in multirate form because of limitations in sensors, control law processor capabilities, or signal bandwidth issues. Furthermore, most standard techniques for approximating continuous transfer functions with digital implementations fail to properly characterize the continuous response, even up to the Nyquist frequency. For example, the F/A-18 RFCS longitudinal control system (fig. 6) has an 80-Hz pitch-rate feedback loop combined with 40-Hz AOA, and the lateral–directional control laws combine roll rate at 80 Hz with a 40-Hz yaw rate, lateral acceleration, and sideslip rate. For the ASE analysis, in which modal frequencies are near and significantly above the Nyquist frequency, multirate discretization becomes an important consideration because of aliasing effects. Hence, particular attention is given to these topics for the F/A-18 HARV TVCS analyses (Appendix B). Figure 14 shows the multirate system realization.

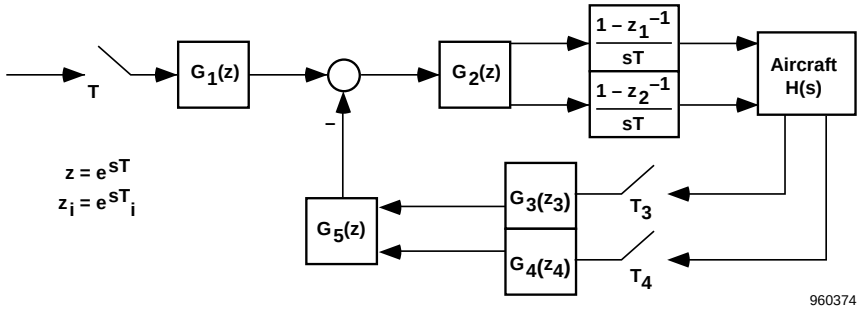

(a) Hybrid.

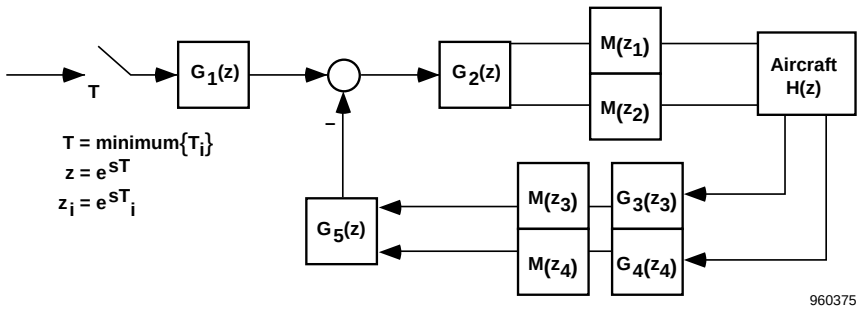

(b) Fast-rate.

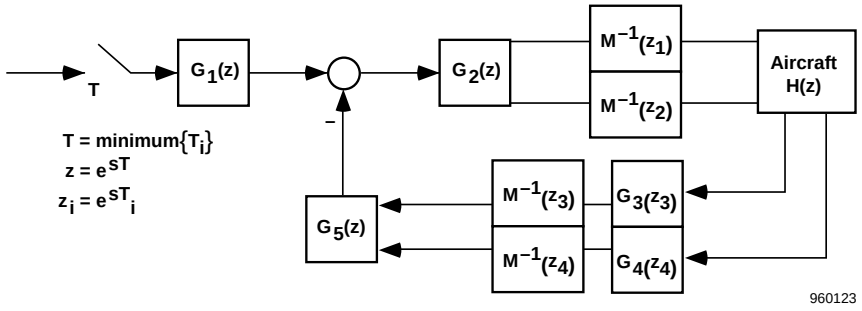

(c) Slow-rate.

Figure 14. Multirate combined system realizations.

Closed-Loop Ground Test

When the modeling process was completed, ground tests were constructed to compare closed-loop combined system behavior with analyses. Closed-looped tests are critical for examining dynamic coupling before aerodynamic augmentation. A flight condition of Mach number 0.2, at an altitude of 30,000 ft, with a 40° AOA (to compute control law gains) was chosen for the basic control law combined system ground test because it is a relatively high-gain condition at high AOA. Closed-loop responses were derived by individually summing sinusoidal sweeps up to 20 Hz into each command loop. Figure 15 compares closed-loop responses between the predicted and test data for input signals injected into the aileron loop for the heavy-weight aircraft. Based on such correlations, the analysis model was used to predict ASE characteristics for basic control laws and RFCS.

Analysis Results

A gain stabilization criteria of 6-dB peak clearance at and above the frequency of the first structural mode, with no phase margin requirement, has been an accepted design goal for classical loop gain robust stability (refs. 2 and 15) when flexibility is considered in the presence of unmodeled uncertainty. However, the multivariable stability margin, μ, (ref. 16), which accounts for structured or unstructured model uncertainty in all loops at each frequency, is a more indicative measure of robust stability. The multivariable margin is able to check stability levels at various locations in the feedback structure (usually at the plant inputs, sensor outputs, and regulated variable error points) to determine if the control laws result in a stable closed-loop system for all reasonable true systems, given the nominal model and uncertainty bounds. These uncertainty bounds can be reliably estimated (refs. 17 and 18) based on previous experiences and particular model fidelity. Therefore, besides the common single-loop-at-a-time gain stabilization checks on robust ASE stability, multivariable loop gain rolloff criteria were also addressed. In general, open-loop eigenvalues, closed-loop roots, loop gains, and multivariable margins should be routine calculations necessary for stability analysis.

Figure 16 shows sample equivalent open-loop responses for longitudinal, lateral, and directional loops for both controllers at the test condition. The plots on the left side of this figure show responses for heavy weight aircraft. The responses for lightweight aircraft are shown in the plots on the right side. Differences between basic and RFCS configurations are most significant in the lateral plot. RFCS lateral loop gains seem to be a potential problem at this high-gain condition. The analysis, including the aerodynamics, was performed at a dense array of flight conditions to study the RFCS ASE properties in all axes.

The multivariable complement of the classical gain and phase margin criteria used for single-loop-at-a-time analysis is the multivariable margin, commonly referred to as μ. This measure captures the performance and stability aspects of feedback reliably and nonconservatively for multiple loops simultaneously in the presence of uncertainties. Furthermore, the multivariable margin encompasses the realistic situation of uncertainty that occurs anywhere in the loops in a structured manner, not just arbitrarily. The ability to treat simultaneous structured uncertainties also offers the ability to deal with performance and robustness concurrently. Although stability and performance evaluations with perturbations dealt with individually can have good results, μ analysis gives necessary and sufficient conditions for stability in the face of multiple, simultaneous, and bounded perturbations of fixed but arbitrary structure.

In practice, conditions imposed on nominal feedback loop shapes depend on where and how the generally complex perturbation, Δ, enters the system. Multiplicative perturbations on the open-loop plant G, described by $\acute{G} = (I + \Delta)G$ at the output, or $\acute{G} = G(I + \Delta)$ at the input, represent uncertainty characterized by sensor and actuator errors, or neglected high-frequency dynamics. These perturbations impose constraints on the complementary sensitivity functions. Alternatively, output ($\acute{G} = (I + \Delta)^{-1}G$) and input ($\acute{G} = G(I + \Delta)^{-1}$) sensitivity representations characterize low-frequency plant parameter errors. The type of uncertainty description imposes a condition on the nominal feedback loops for robustness and performance. The plant parameter errors, in

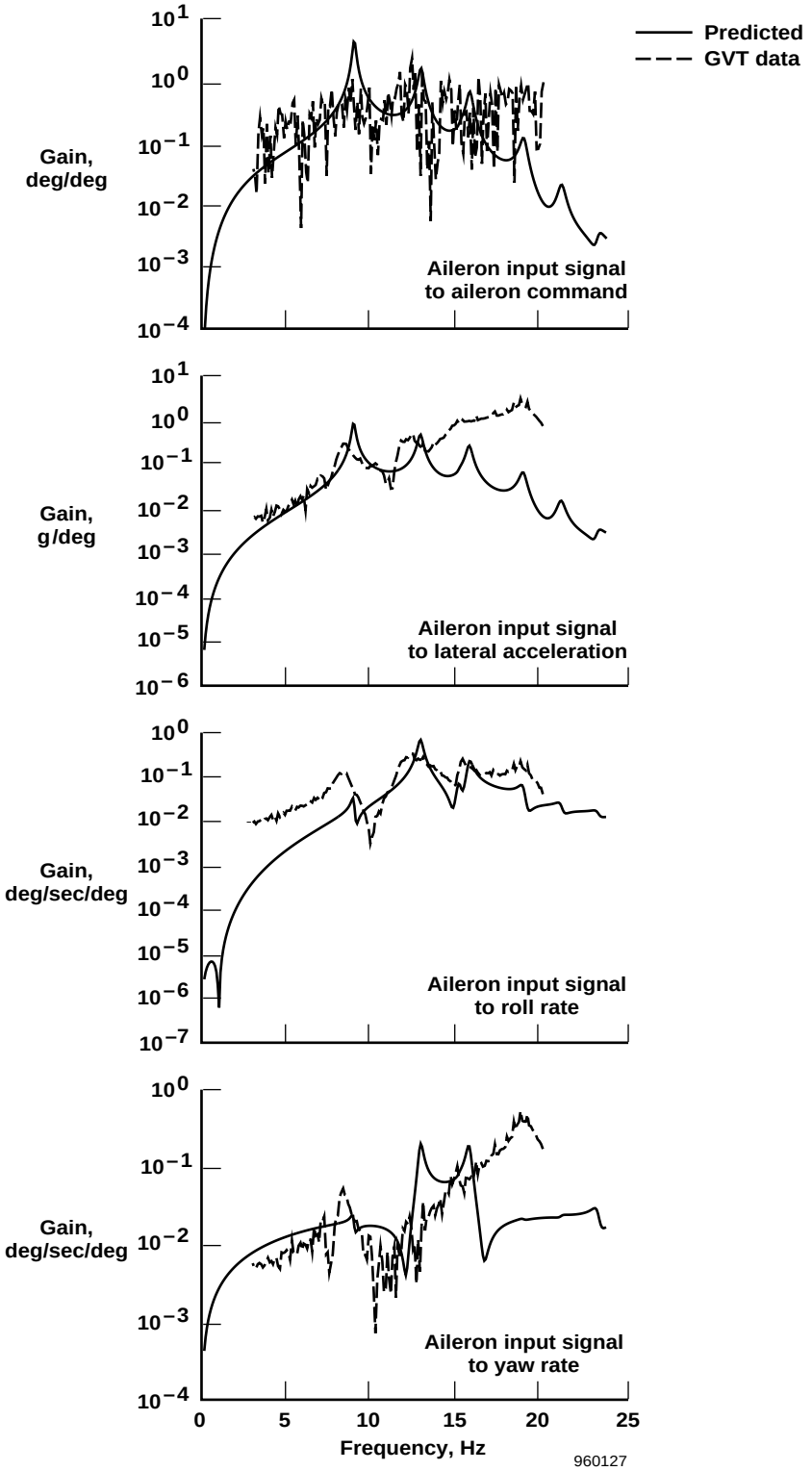

Figure 15. Comparison of predicted data with GVT data for aileron closed-loop responses.

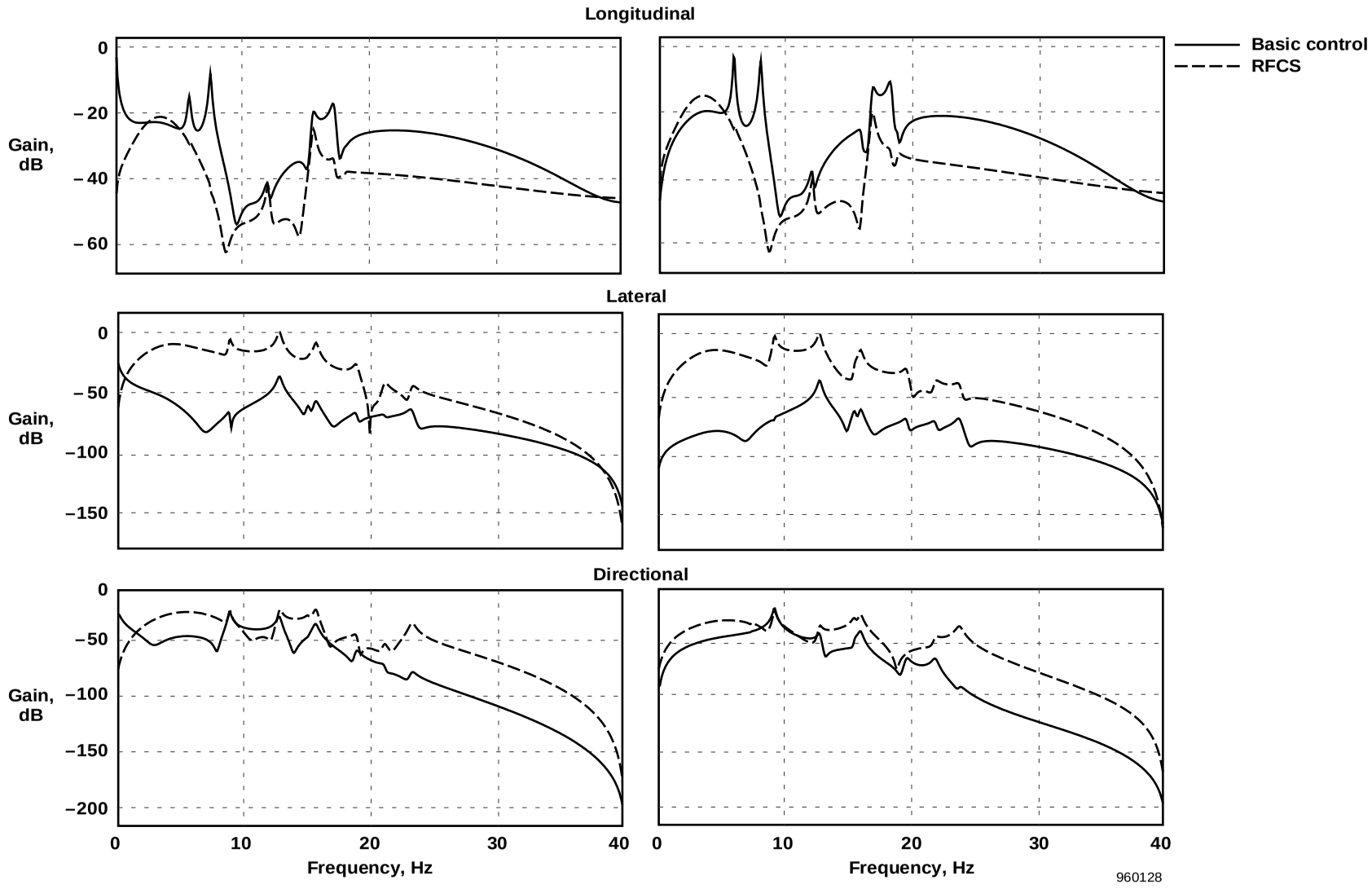

Figure 16. Comparison of basic control law and RFCS loop gains at Mach 0.2, altitude 30,000 feet, 40° AOA test configuration.

turn, impose constraints on the sensitivity functions. In an experimental setup, external signals can be used to derive the necessary multivariable transfer functions that reveal how uncertainty enters the system as compared to the nominal analysis model, and expose system anomalies as well as potential stability and performance problems. This setup was used for ASE stability monitoring in this study. In addition, all robust stability tests are for complex diagonal perturbations at desired loop points, because these perturbations are physically motivated and nonconservative.

Figure 17 shows structured singular values of the complementary sensitivity at input (actuator) commands and output (sensor feedback) points for a sample lateral–directional case at 45-lb/ft^2 dynamic pressure and 70° AOA. The behavior depends on where the uncertainty enters. These plots can be interpreted much like loop gains in a single-loop system, but here the lateral and directional loops are examined simultaneously. In addition, the –6-dB gain stabilization criterion is assumed to be the robust stability guideline for multiloop analysis as well. Hence, at the first antisymmetric wing-bending mode frequency of 9 Hz and the wing torsion frequency of approximately 12.5 Hz, peak values near 1 (0 dB) indicate poor stability robustness.

Figure 18 shows equivalent open-loop responses taken from the longitudinal, lateral, and directional loops at the same condition. For describing the aerodynamics of the F/A-18 HARV TVCS in state-space form, the Padé fits to the doublet-lattice aerodynamics were designated zero order to simplify the aerodynamics. The objective was to incorporate the higher order actuator models and still maintain a reasonable order model. The justification is based on the premise that at higher AOA and low dynamic pressure, the modal dynamics are predominantly servoelastic, so more emphasis is invested in the well-defined actuation characteristics. The plots in figure 18 show that the simple zero order Padé fits for the unsteady aerodynamics give responses nearly identical to those using second-order fits, thereby substantiating the presumption that the order of the Padé fits can be reduced at typical high-AOA conditions. In the lateral response, the modal gain peaks for the same two antisymmetric wing modes that exhibited poor robustness levels are near 0 dB and the accepted gain stabilization criteria of –6 dB is exceeded. These individual loop gains yield optimistic stability margins compared to the multiloop margins shown in figure 17.

Other flight conditions revealed even lower stability levels, but in all cases analyzed inside the flight envelope, the corresponding closed-loop dampings at these modal frequencies never predicted an actual instability. An eigenvalue analysis did not disclose any potential instabilities, but the hybrid frequency results obviously showed a potential problem for the two antisymmetric modes at high-AOA and low-dynamic-pressure conditions in RFCS. The origins of the possible hazard were investigated and found to be mainly from the lateral acceleration feedback. Instead of expending time to devise, implement, and test notch filter adjustments or additions to lower the loop gain at these modal frequencies, (with possible sacrifices in rigid-body stability and/or handling qualities), a flight plan was devised to cautiously expand the flight envelope to verify safety of flight.

FLIGHT TEST TECHNIQUE

Excitation and Instrumentation

One concern for safe envelope expansion at high AOA is the requirement for an adequate signal-to-noise ratio to discern modal response from a noisy environment. Buffet pressures exhibit wide-band frequency response characteristics with preferential frequency bands, depending on AOA. The frequency range of the dominant pressure response for a particular AOA determines which modes receive the greatest excitation. References 19 through 21 outline some buffet characteristics for an F/A-18 aircraft. Buffet excitation is greatest between 20° and 50° AOA, which may have adverse effects for stability estimation because it is an unmodeled external input. Such considerations led to the design of an onboard excitation system (OBES). This system was implemented by summing signals to actuator commands for structural excitation (figs. 5, 6 and 7).

Frequency sweeps were generated to command a particular control surface to induce sufficient inertial and aerodynamic loading to the aircraft. Sweeps from 5 Hz to 20 Hz were added to the stabilator, aileron, rudder, pitch vane, and yaw vane commands to encompass the modal dynamics of the first-bending and torsion modes

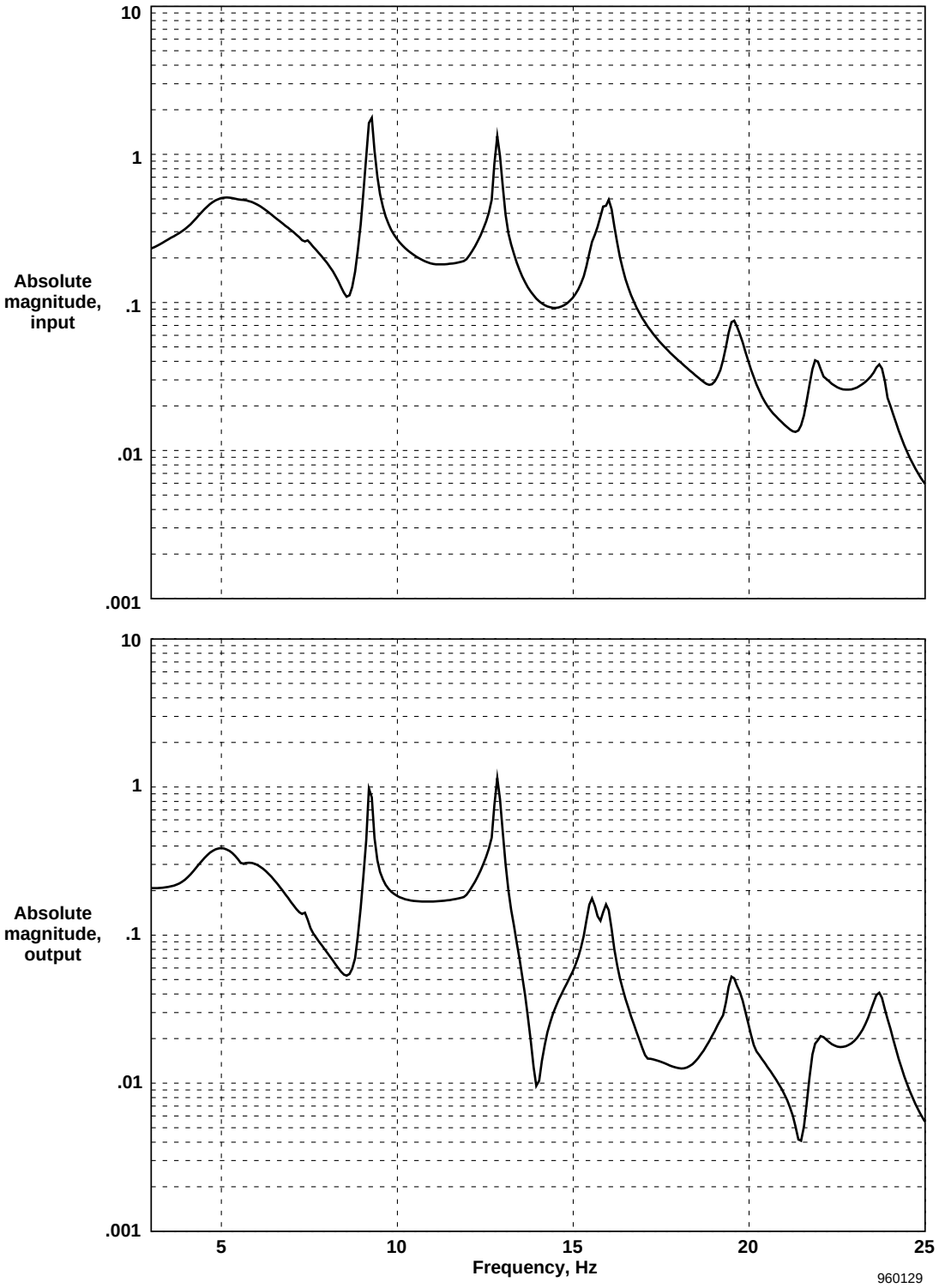

Figure 17. Predicted lateral–directional complementary sensitivity structured singular values at input and output for high AOA of 70° and dynamic pressure of 45 lb/ft^2.

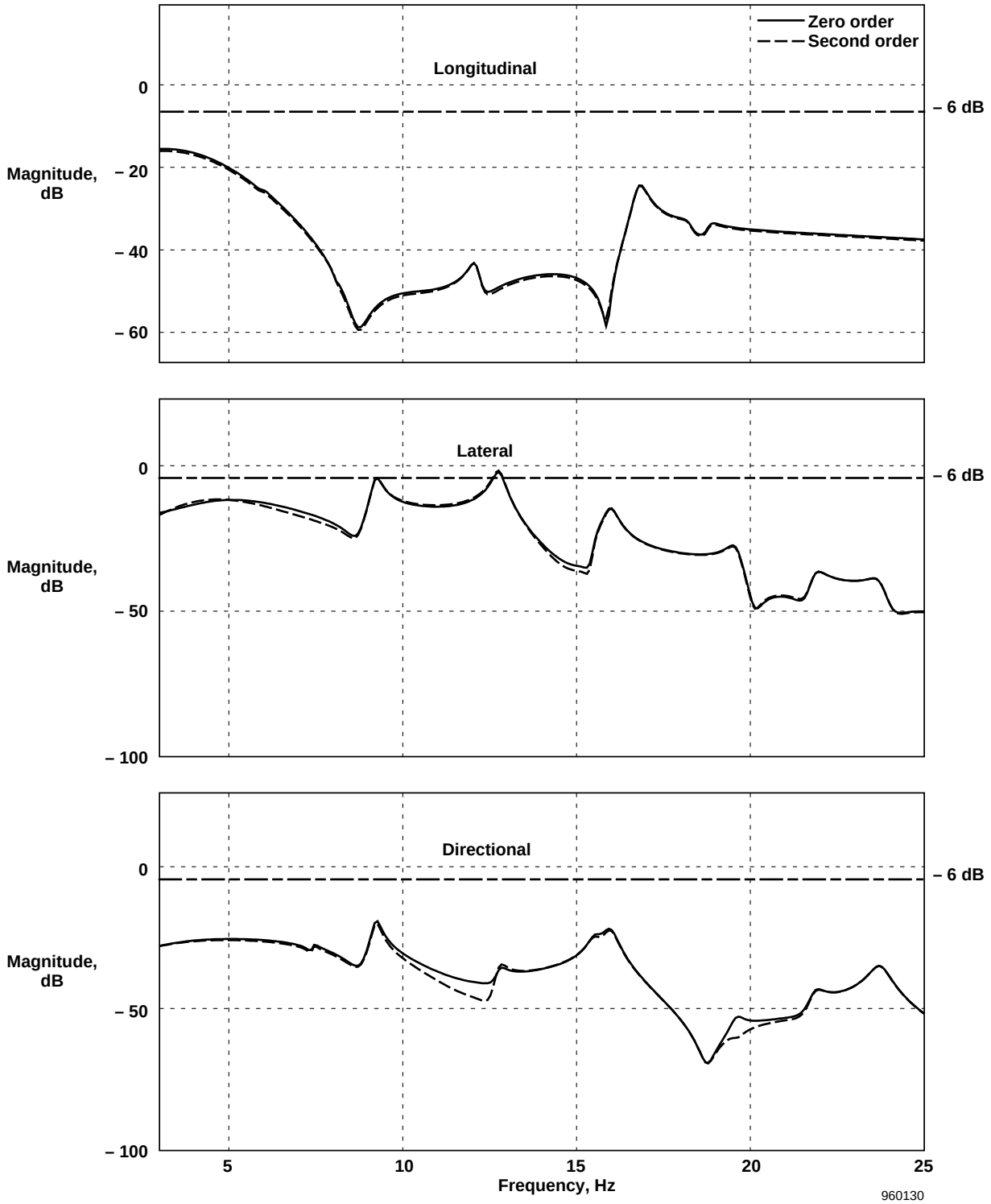

Figure 18. Comparison of zero-order and second-order unsteady aerodynamic fit in the RFCS loop gains at high AOA of 70° and dynamic pressure of 45 lb/ft^2.

in each axis. Although aerodynamic surfaces are good sources of excitation for low AOA, at higher AOA the vanes provided inputs to supplement the ailerons because the rudders became relatively ineffective and the stabilators were saturated.

Instrumentation consisted of accelerometers mounted on the wing tips, horizontal stabilators, vertical stabilators, ailerons, and fuselage. Feedback measurements to the control system and angular accelerometers mounted in the fuselage were used to analyze the flight data for ASE properties. ASE clearance was achieved by concentrating on fuselage sensors because the feedback signals were measured here, and the linear and angular acceleration measurements tended to give higher quality data for modal response than rate gyros.

AOA Envelope Clearance

A flight plan was devised based on the analysis to establish a dynamic pressure and corresponding AOA trend in damping estimates. That is, for each dynamic pressure down to 60 lb/ft^2 there was a related AOA for level trimmed flight, regardless of altitude, so that trends in dynamic pressure were correlated with trends in AOA. Effects of density variation were insignificant. For lower dynamic pressures and AOA greater than 20°, a constant AOA was maintained for each series of sweeps while sacrificing altitude. Figure 19 shows AOA clearance, which started at 170 lb/ft^2 dynamic pressure, 5° AOA, at three different altitudes, then moved to 100 lb/ft^2 dynamic pressure, 10° AOA, followed by 60 lb/ft^2, 20° AOA, until it reached 30–45 lb/ft^2, 30° AOA. Subsequent AOA clearance required testing 10° increments up to 70° AOA. At the initial low-AOA test points, all the surfaces were excited to refine the choice of excitation mechanisms and amplitudes until a small subset was chosen for high-AOA clearance.

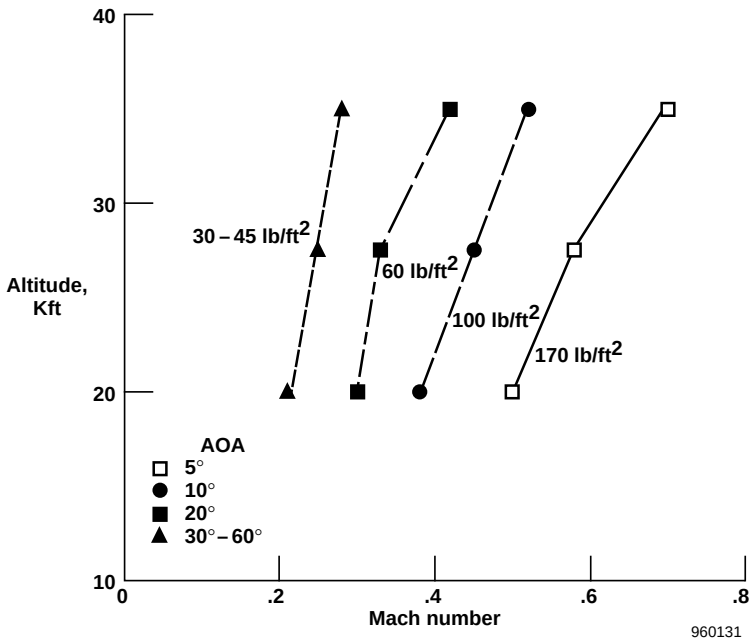

Figure 19. F/A-18 HARV TVCS aeroservoelastic clearance conditions for high AOA.

Upon engaging the OBES during the first envelope clearance flight, yaw and roll coupling during the yaw vane commanded sweeps appeared to such a degree that the pilot aborted the sweep just before 20 Hz. The tail end of the sweep (fig. 20) exposed the interaction as the rudder and yaw vector commands responded to yaw rate and lateral acceleration when the sweep varied from 17 Hz to 20 Hz. Frequency content decreased linearly from 3 Hz until OBES termination. The concern was that the low-frequency oscillations were diverging and the pilot would lose controllability of the aircraft. This phenomenon is a result of the discretely excited system containing spectral

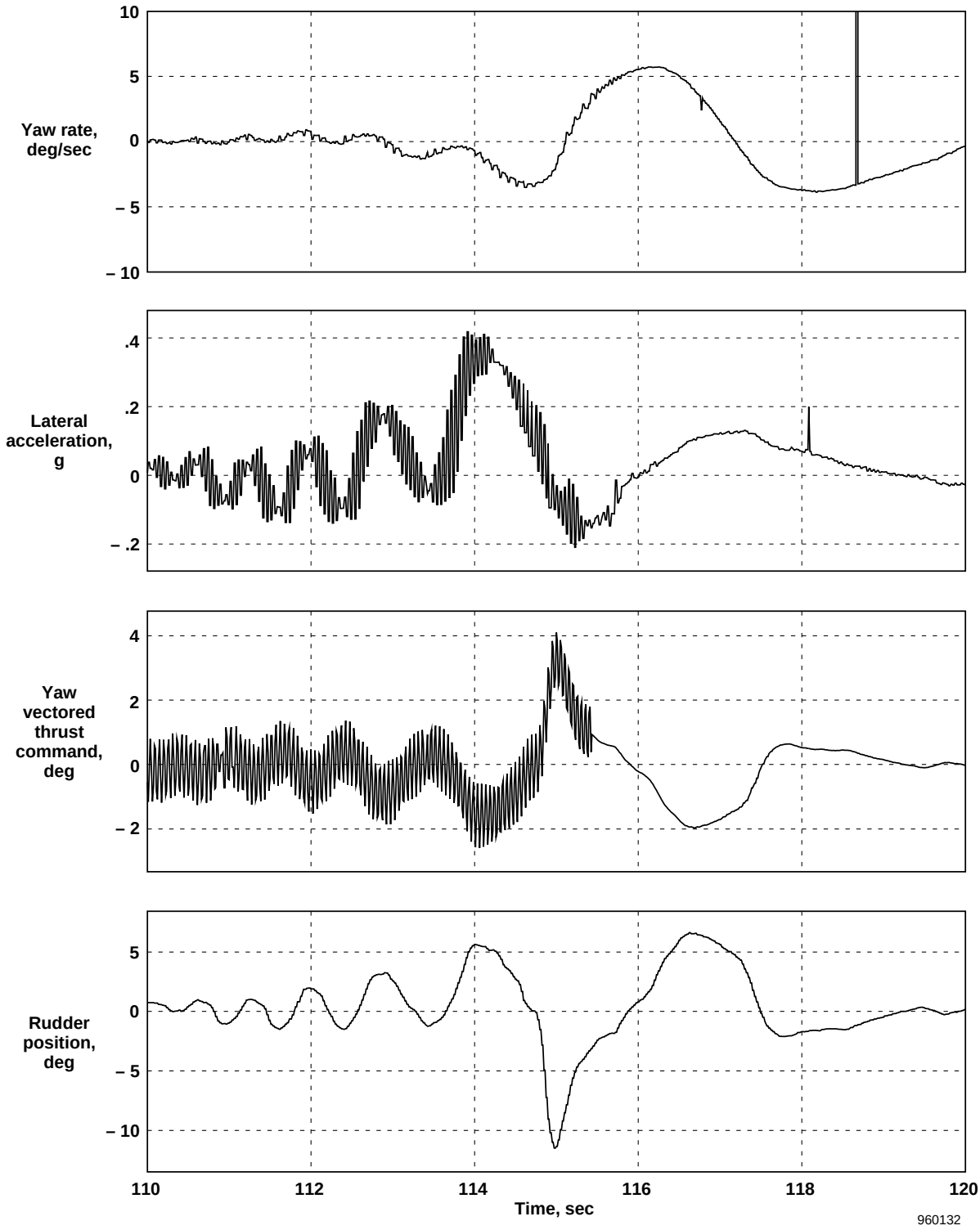

Figure 20. Selected time responses during first commanded yaw-vectored-thrust excitation in flight.

components in the continuous output force at the input frequency and all of its aliases. The alias is at the driving frequency plus the Nyquist frequency. Even though the sweep was run up to only 20 Hz, the first alias of the forcing function was found up to 40 Hz. Furthermore, from this alias, the digital system sensed a component folded down about the Nyquist frequency of 20 Hz and produced a signal of significant power from 3 Hz to 1 Hz. The 40-Hz lateral acceleration and yaw-rate feedback in RFCS lateral–directional control loops responded to the substantially modulated spectral components of the input, resulting in rigid-body coupling. Coupling and vibration levels were excessive enough that amplitudes were decreased for both pitch- and yaw-vectored-thrust commands.

In the following synopsis of feedback properties as functions of AOA, lateral acceleration is regarded as the most critical feedback because it is primarily responsible for poor predicted stability robustness and demonstrates the most sensitivity to changing conditions. Other feedback responses, displayed for informational purposes, are relatively less meaningful in this context.

Aileron sweeps have the most promising antisymmetric excitation effectiveness of the aerodynamic surfaces from the responses at 20° AOA (fig. 21). The trend of lateral acceleration feedback responses as a function of AOA (fig. 22) reveals that modal definition is improved as AOA is increased from 30° to 50°. Furthermore, figure 23 (pitch vane inputs), figure 24 (yaw vane inputs), and figure 25 (ailerons), show no significant adverse trends in any of the feedback signals as a function of AOA. An additional application of the OBES is the generation of transfer functions. Figures 26 and 27 show transfer functions of normal acceleration from pitch vane command and lateral acceleration from yaw vane command. These comparisons support the validity of the model; more appropriately, with a modern behavioral approach to systems, the model is not falsified by the data.

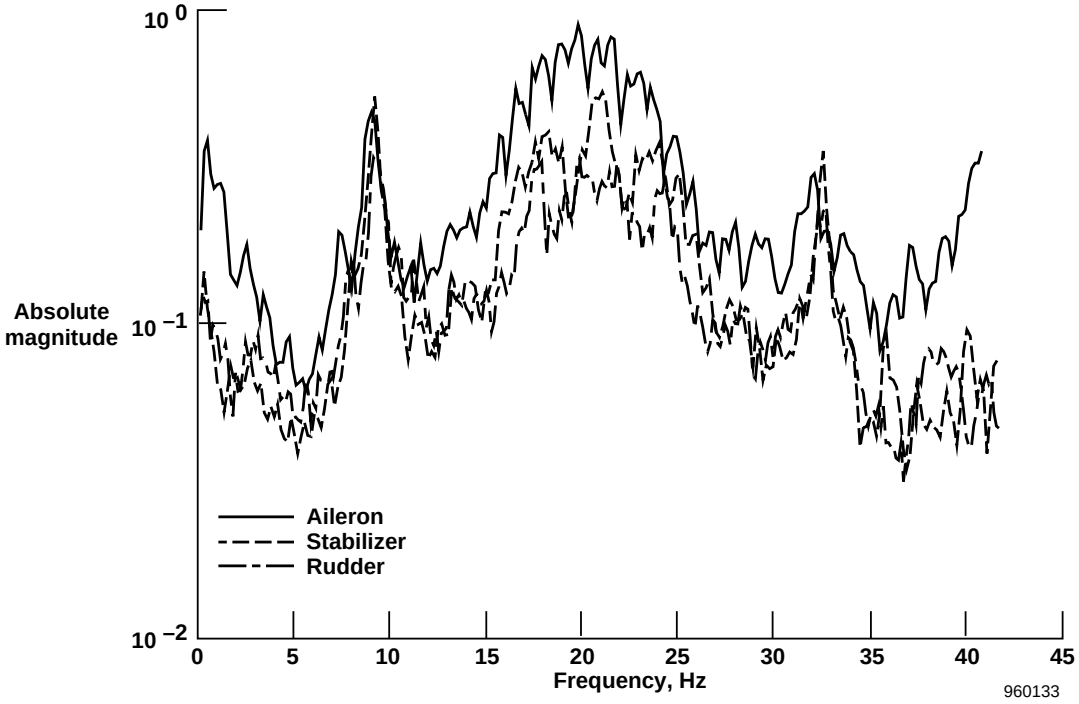

Figure 21. Comparison of lateral acceleration responses from stabilator, aileron and rudder input excitation at 20° AOA.

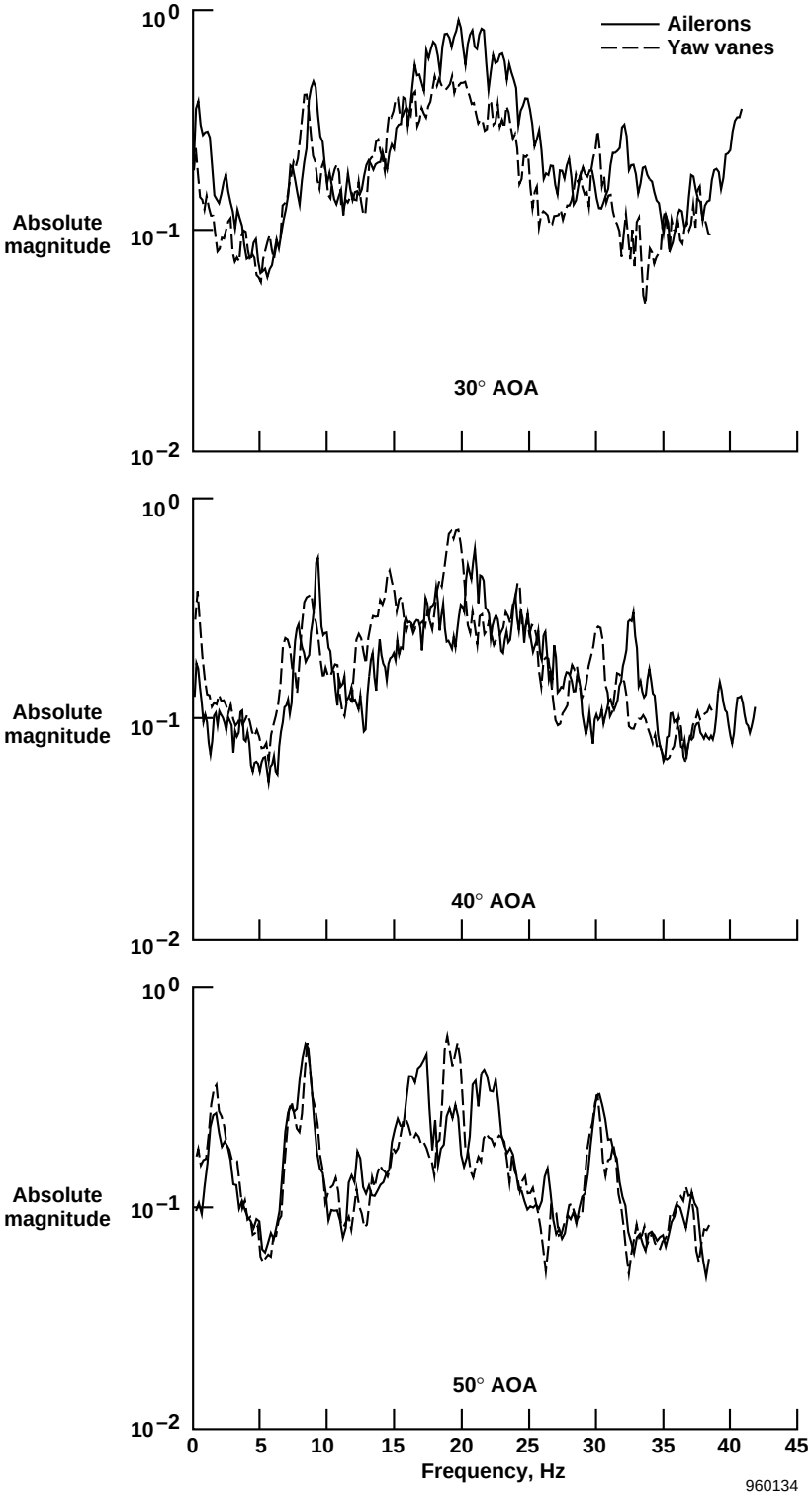

Figure 22. Comparison of flight lateral accelerations feedback from ailerons and yaw vane vectored thrust inputs at 30°, 40°, and 50° AOA.

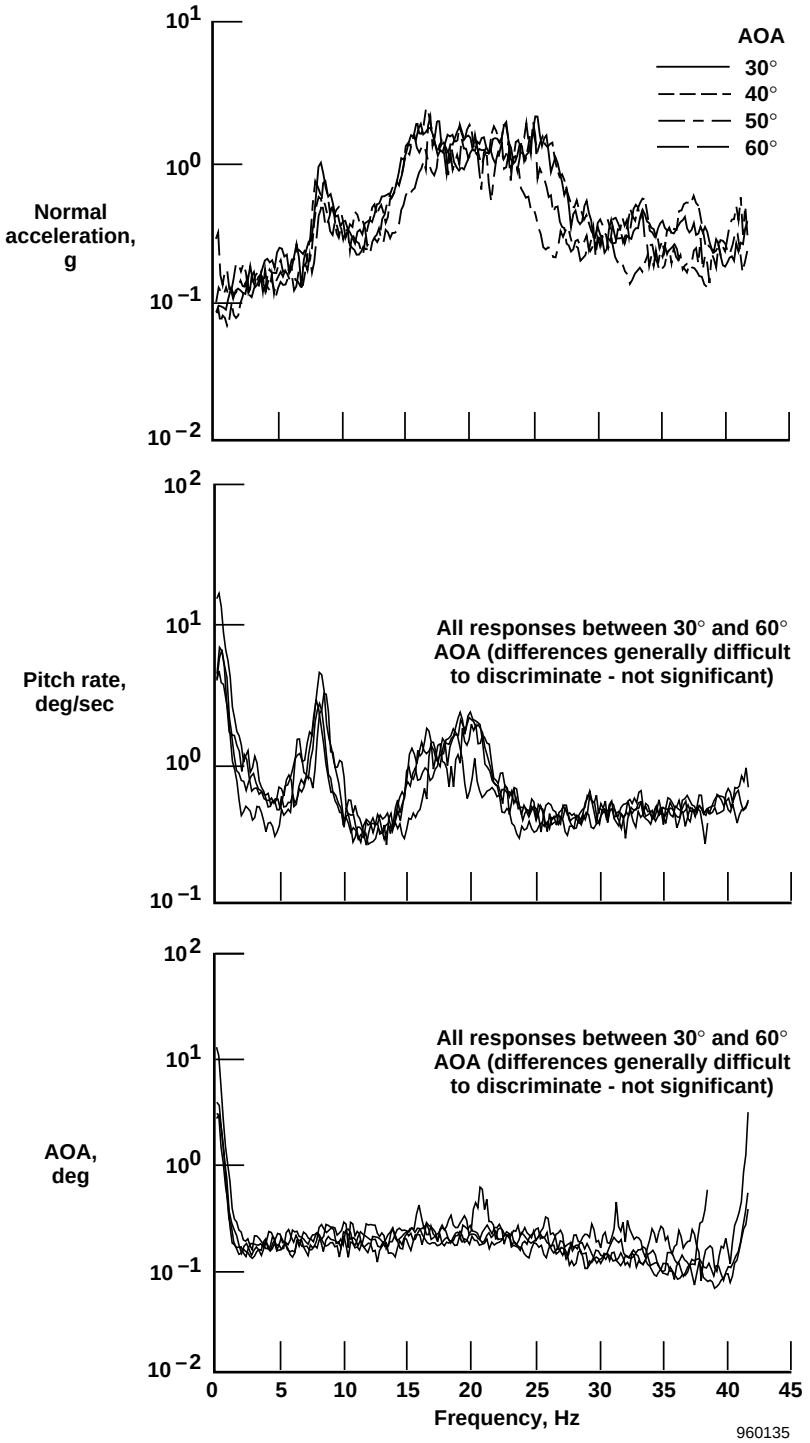

Figure 23. Longitudinal flight feedback responses at 30°, 40°, 50°, and 60° AOA from pitch vane vectored thrust excitation.

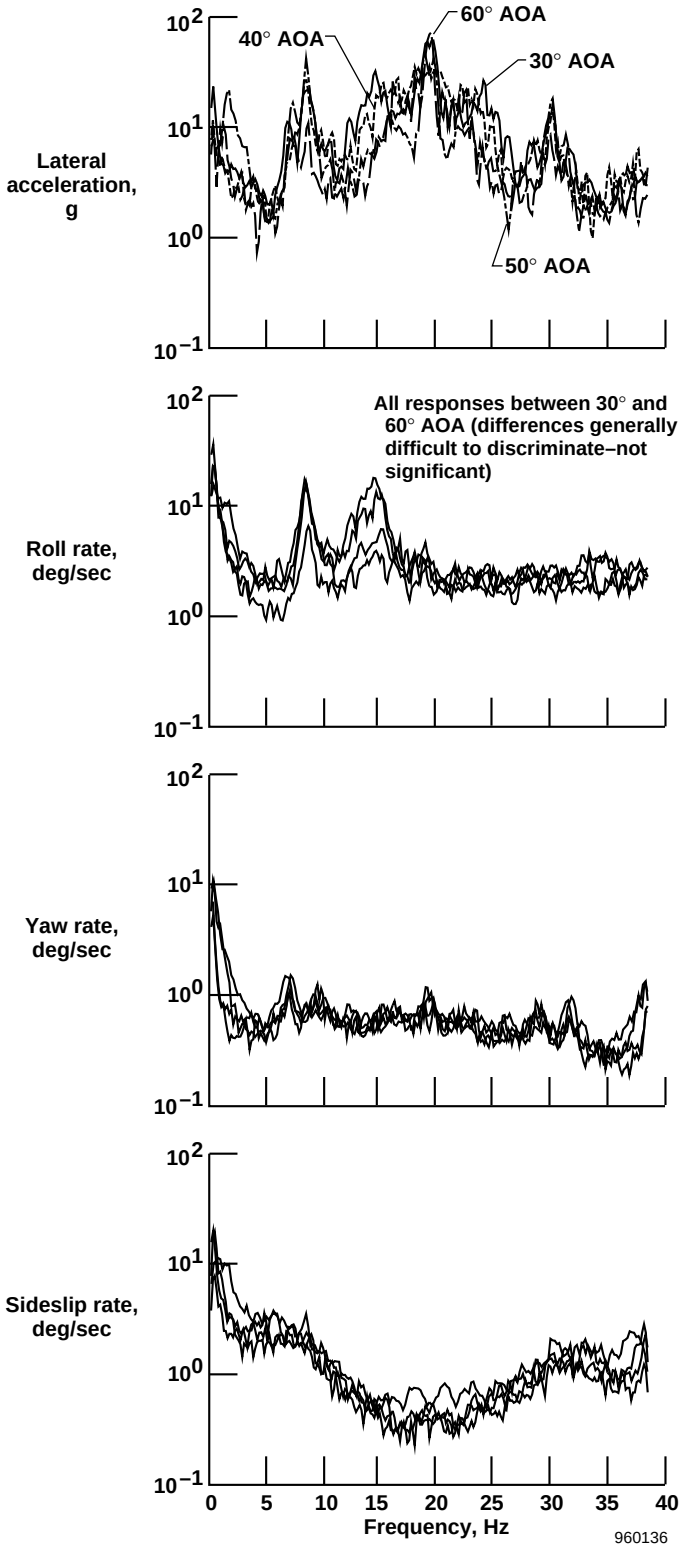

Figure 24. Lateral–directional flight feedback responses at 30°, 40°, 50°, and 60° AOA from yaw vane vectoring thrust excitation.

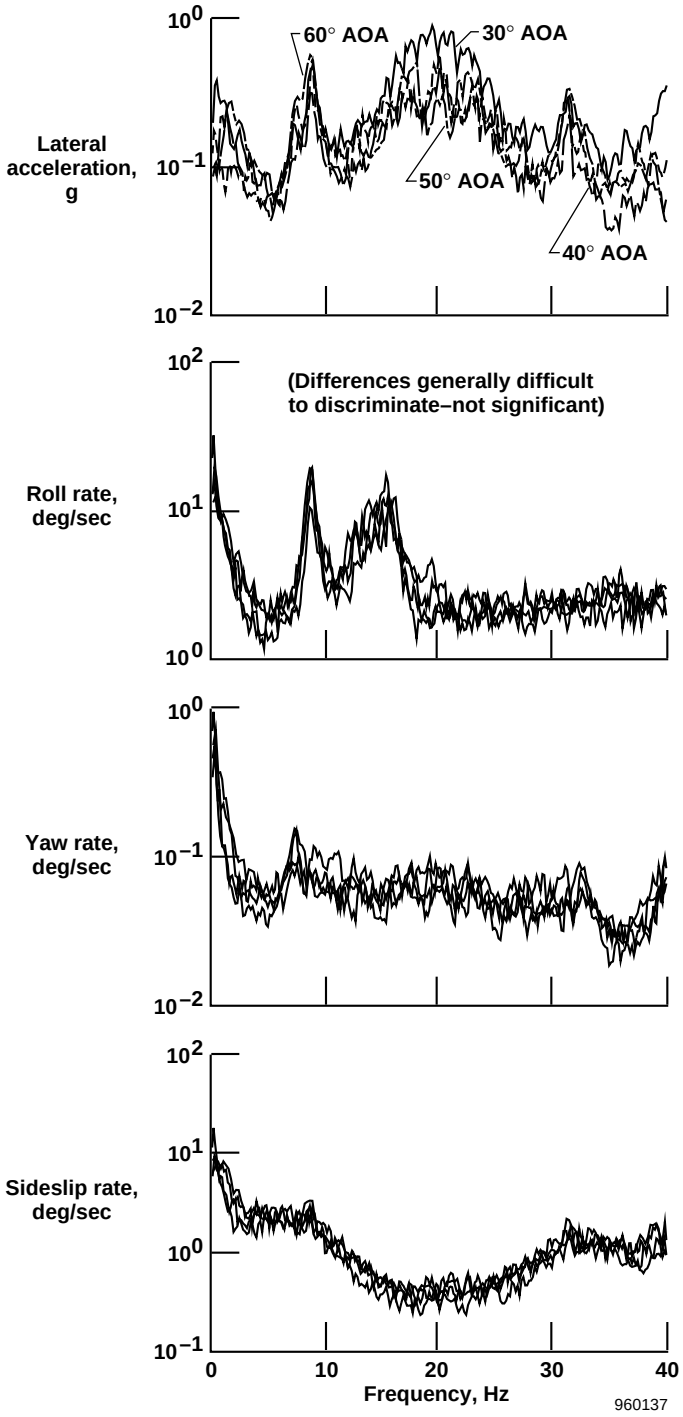

Figure 25. Lateral–directional flight feedback responses at 30°, 40°, 50°, and 60° AOA from aileron excitation.

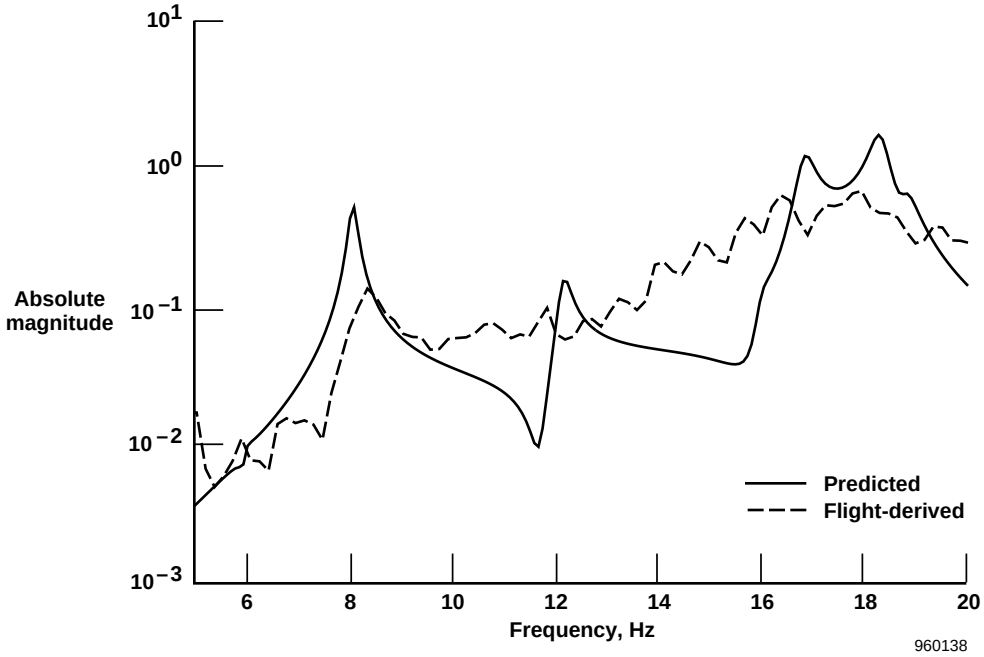

Figure 26. Comparison of predicted and flight-derived transfer function from pitch-vectored-thrust command to normal acceleration feedback at 40° AOA.

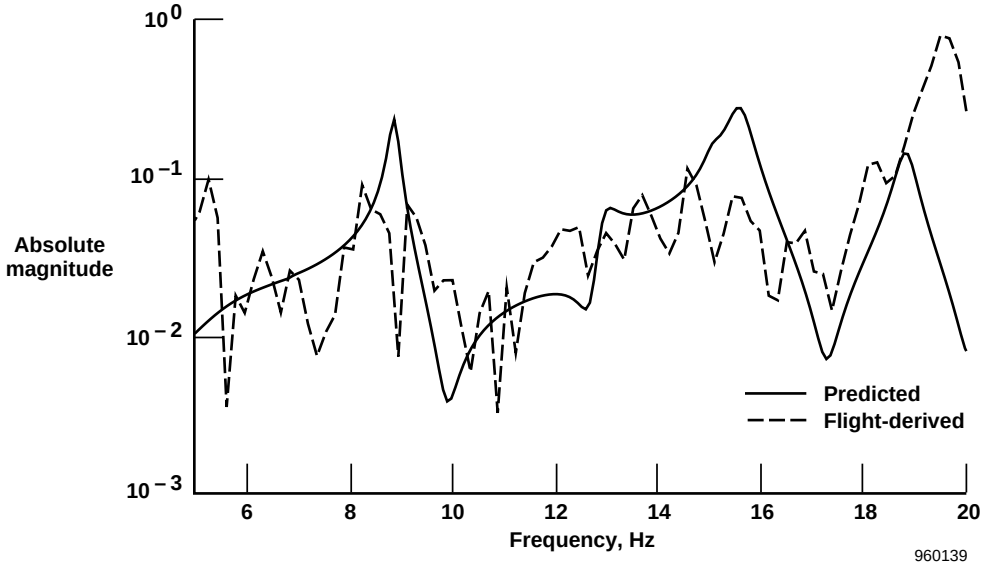

Figure 27. Comparison of predicted and flight-derived transfer function from yaw-vectored-thrust command to normal acceleration feedback at 40° AOA.

STABILITY RESULTS

Frequency and Damping

The following multiple-degrees-of-freedom (MDOF) procedure (ref. 22) was used to extract frequency and damping estimates from flight data:

(1) Transform time data (with ensembling, windowing, etc.) to get the magnitude of the signal in the frequency domain.

(2) Generate the phase using the complex cepstrum (inverse transform of the logarithm of the transform).

(3) Choose a frequency range for modal estimation.

(4) Choose an order for the transfer function to fit this frequency range.

(5) Fit a stable minimum phase transfer function to the magnitude data using linear programming.

Various measurements can be assembled before the procedure is applied. Modal frequency and damping result from the estimated transfer function roots. An example of the application of this procedure is shown in figure 28 where magnitude data between 6 Hz and 16 Hz are fit with twelfth- and fourteenth-order transfer functions. The method successfully discriminates closely spaced modes, and damping estimates tend to have small standard deviation. Numerous estimates were computed at each flight condition to determine frequency and damping.

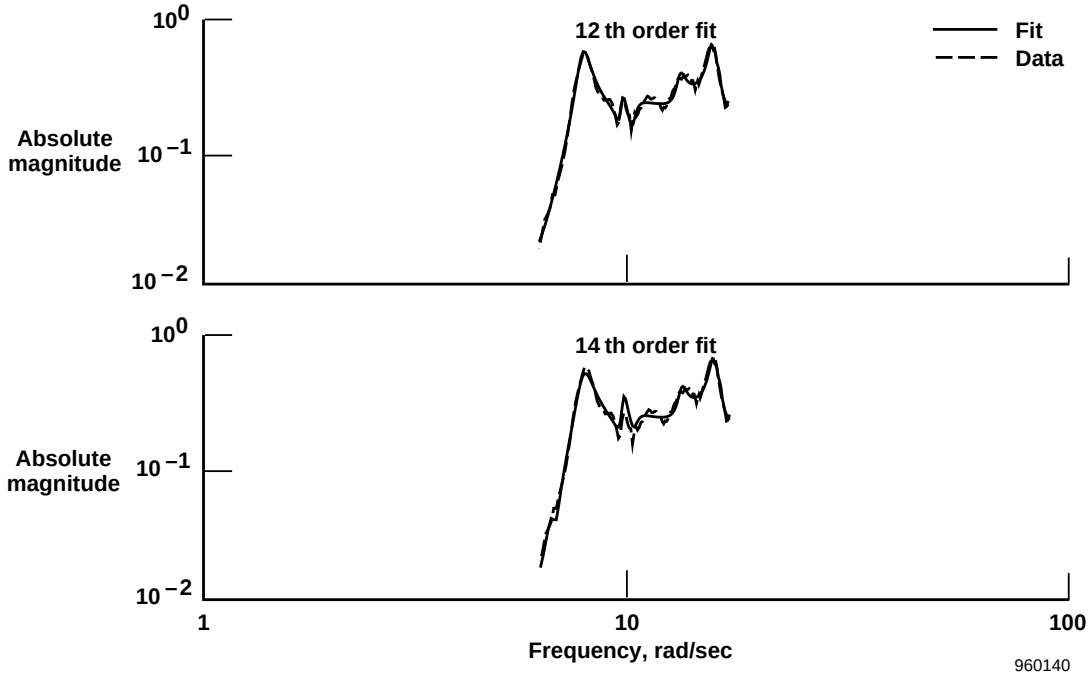

Figure 28. Sample fits using MDOF modal estimation procedure.

Figure 29 shows predicted and estimated modal frequencies as a function of AOA. Predictions are average values of a lightweight and heavy-weight configuration. Frequencies are in excellent agreement; the only noticeable differences are symmetric wing torsion (predicted approximately 0.5 Hz high) and antisymmetric vertical fin (predicted approximately 0.5 Hz low). Figure 30 shows predicted and estimated damping estimates for the modes of interest. The predictions agree reasonably well with the values estimated from flight data, and damping is more

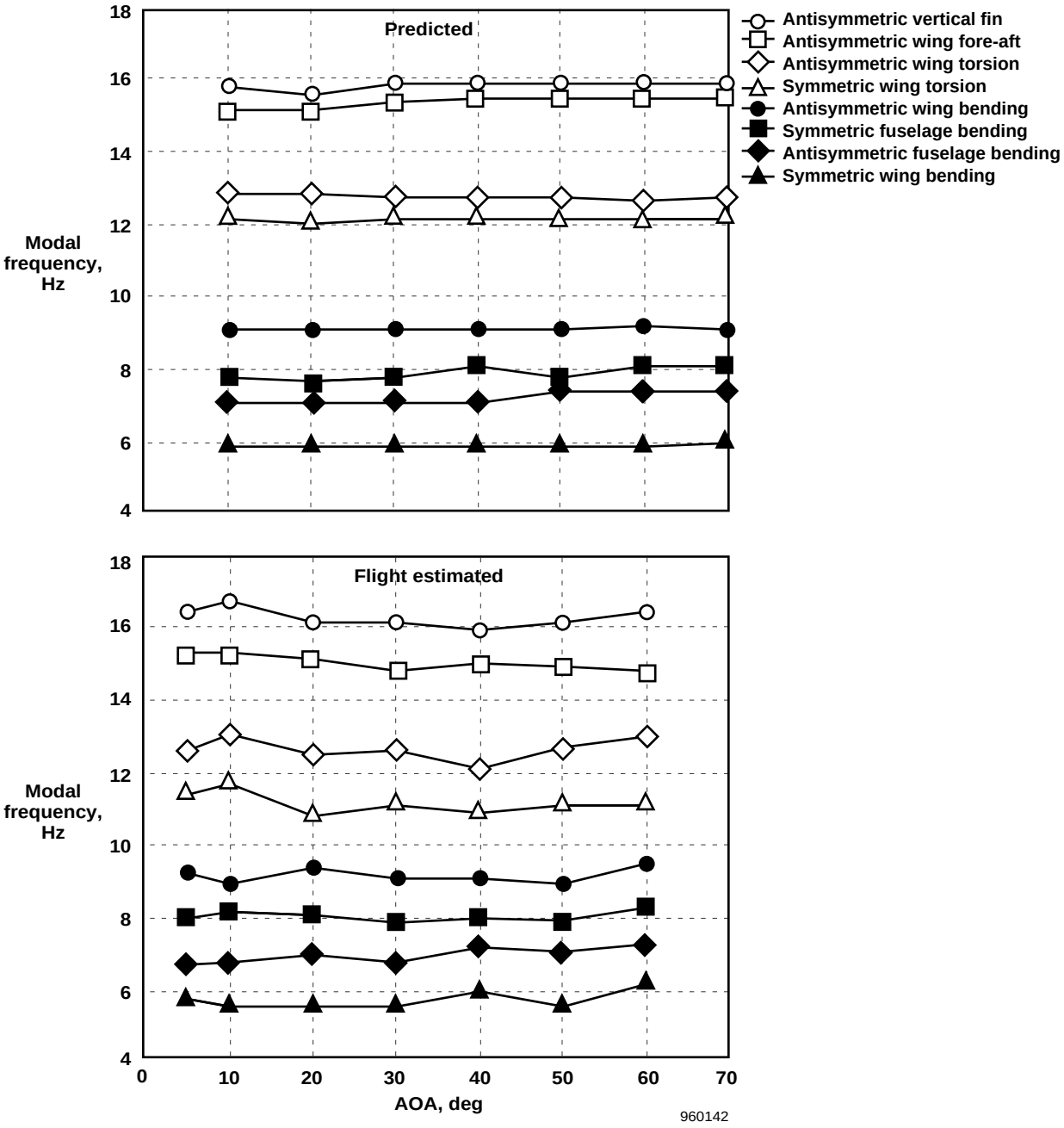

Figure 29. Predicted and flight-estimated modal frequencies of primary modes.

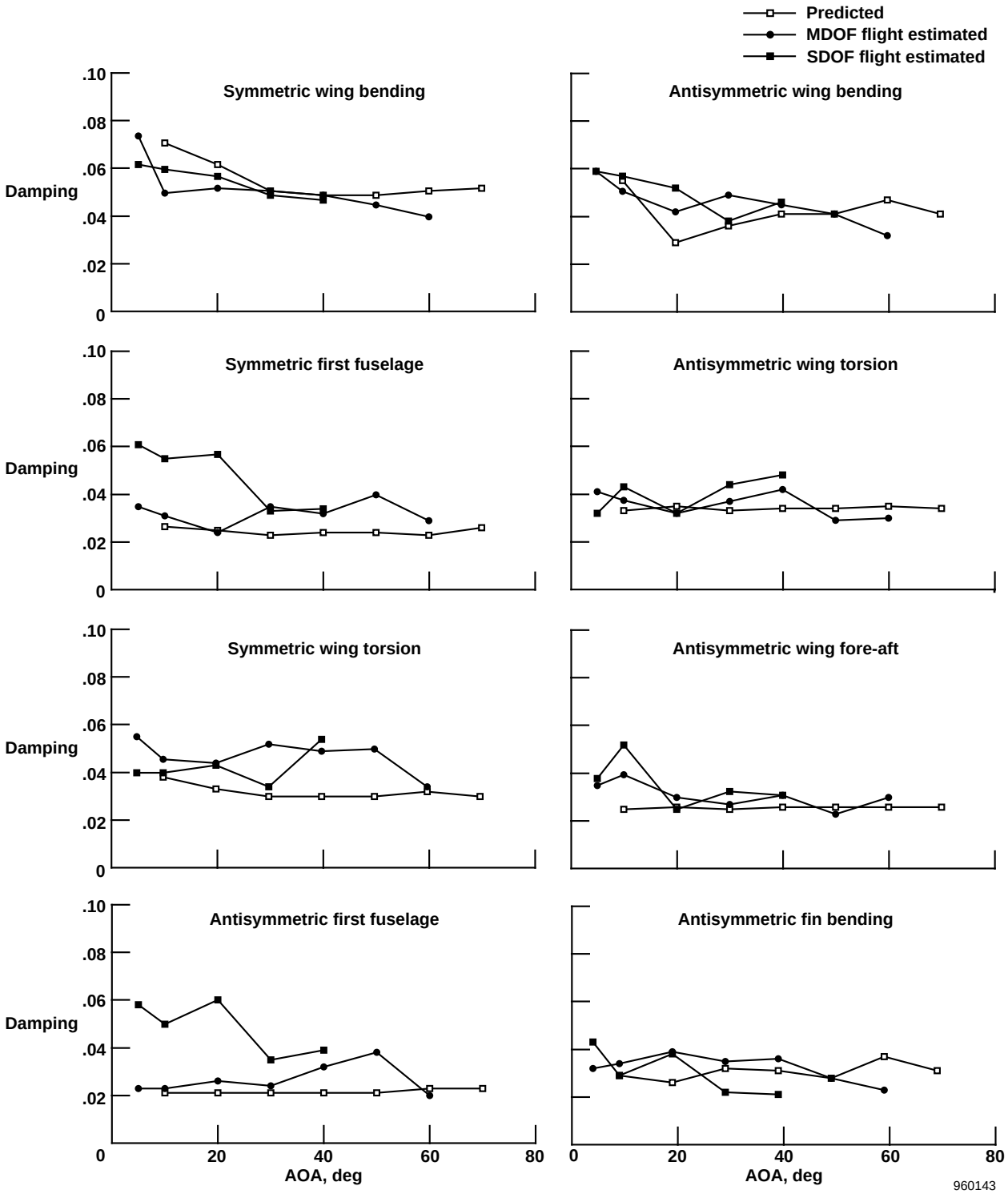

Figure 30. Predicted structural mode dampings compared with flight data estimation results as a function of AOA for primary modes of interest.

than adequate for all the modes. Furthermore, the damping values show no significant adverse trends as a function of AOA (or dynamic pressure) within the RFCS flight envelope. An interesting similarity with the X-29 results (fig. 8) is that the predictions are generally conservative for both aircraft, yet any other resemblance in trends with AOA is not evident.

Transfer Functions and Multivariable Stability

Open Loop

Model validation includes the comparison of predicted and flight-derived open-loop responses from surface commands to feedback sensors. Open-loop response correlations between predictions and flight data vary significantly depending on feedback, surface command, and flight condition. Figure 31 shows open-loop responses from differential stabilator, aileron, rudder, and yaw vectored-thrust commands to lateral acceleration feedback at 5° AOA. Lateral acceleration is overpredicted from differential stabilator and yaw-vectored-thrust commands, and underpredicted from the rudder command. The aileron comparison is a relatively good match, but even with OBES excitation at low AOA, the data quality is not exceptional. At another flight condition, these comparisons could look much different. Since stability is the primary concern, this difference in data quality can be alleviated by concentrating on the multivariable aspect of the system.

Figure 32 shows the physical uncertainty of the plant G without feedback. The unstructured perturbation block Δ represents a complex variation in the plant, so the perturbed plant $\acute{G} = (I + G\Delta)^{-1}G$ is a measure of output errors caused by input commands and disturbances. A computation of the structured singular value $\mu_{\Delta}(G)$ produces the minimum perturbation Δ that causes instability of G, the open-loop aircraft (ref. 23). A comparison of the minimum flight-derived Δ with the minimum predicted Δ that causes feedback loop instability produces a multivariable assessment of the relative instability of the open-loop airplane and model. The minimum Δ is simply the norm of the Δ that causes instability, or the stability margin for the type and location of an uncertainty. A smaller value for the stability margin indicates less robust stability. This feedback interpretation of the structured singular value $\mu_{\Delta}(G)$ is useful for investigating the important multivariable aspects of stability.

Figure 33 shows longitudinal open-loop unstructured minimum Δ's for various AOA as comparisons between flight-derived and predicted computations. Matches between 5 Hz and 20 Hz validate the longitudinal stability predictions, which adds a degree of confidence to the damping results. An unexpected decrease in robust stability is distinct between 9 Hz and 10 Hz at 60° AOA; this decrease is attributed to the pitch-rate gyro sensing significant motion from antisymmetric wing bending.

Because only aileron and yaw-vectored-thrust OBES commands were lateral–directional inputs for 30° AOA and above, these commands and all feedbacks were used to compute the minimum Δ. Lateral–directional open-loop unstructured minimum Δ's are displayed in figure 34. Similarly to the longitudinal cases, the predictions seem insensitive to AOA, but the flight results vary. Fin bending and wing fore-aft near 15 Hz occur most conspicuously at the 30° and 40° conditions where buffet is prevalent. A noticeable change in antisymmetric wing first-bending frequency occurs near 9 Hz between 50° and 60° AOA. At these frequencies, the flight data tend to be less robust than the model between 30° and 50° AOA. This phenomenon may result from buffet loads because at 60° AOA (outside the buffet region) the correlation of robust stability estimates clearly improves. Because the frequency shift at 9 Hz also occurred in the open-loop longitudinal plots at 60° AOA (fig. 33) this shift is likely caused by significantly different wing airloads when going from 50° to 60° AOA. This frequency shift can also be seen in the estimated frequency plots (fig. 29).

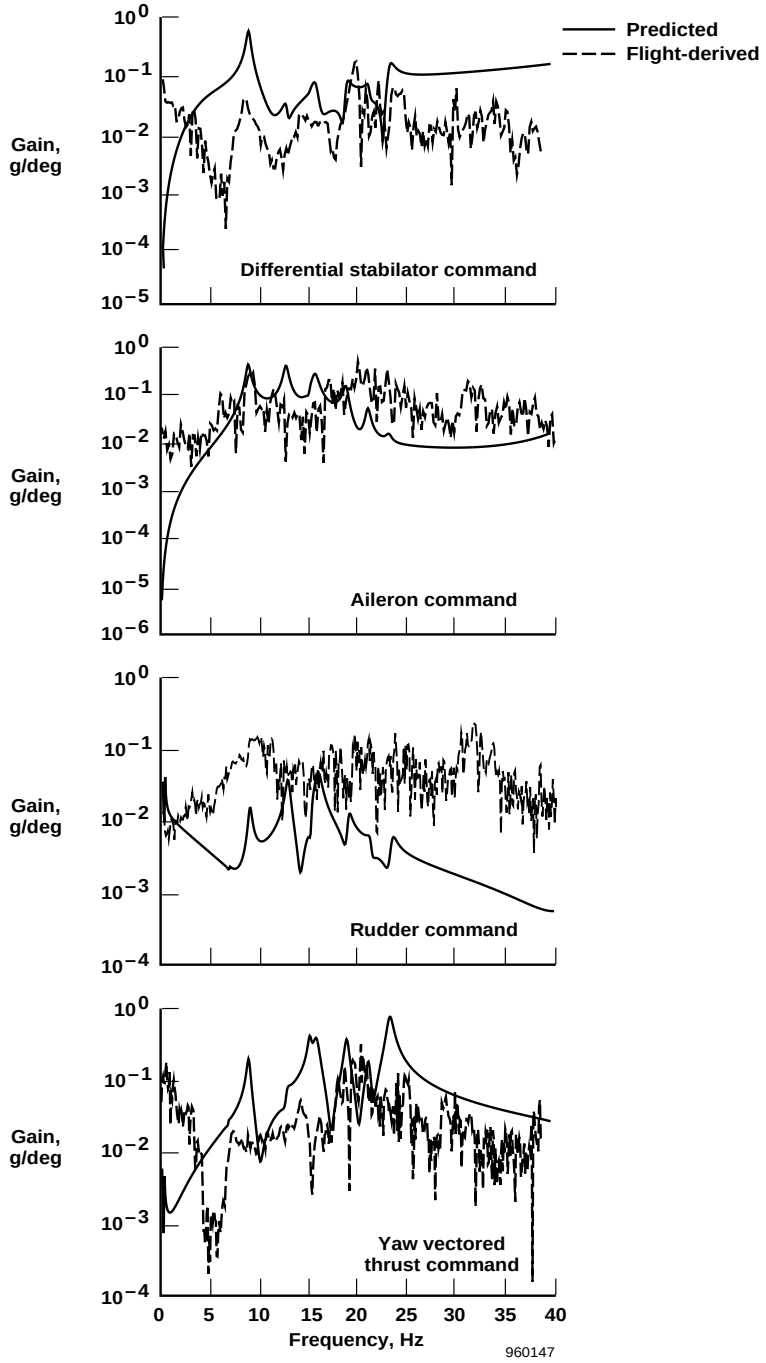

Figure 31. Predicted and flight-derived open-loop transfer functions from control-surface commands to lateral acceleration feedback at 5° AOA.

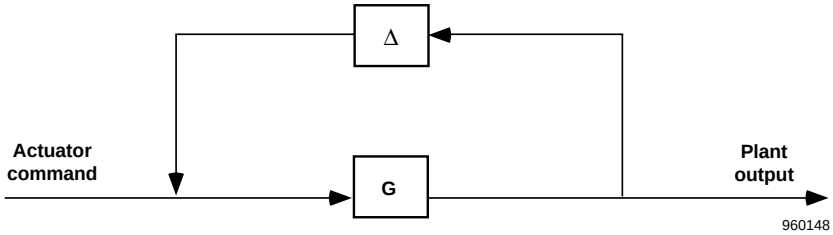

Figure 32. Open-loop uncertainty description of output errors due to input commands and disturbances.

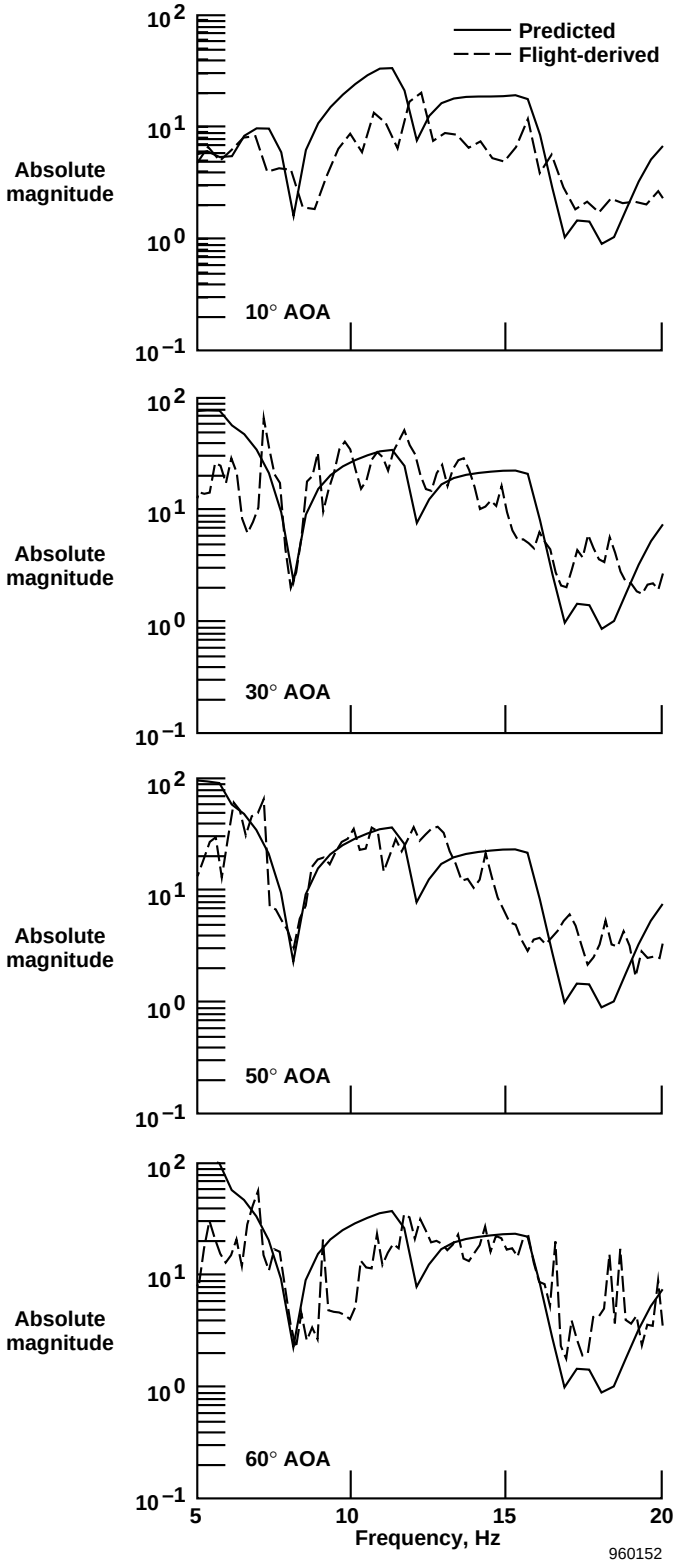

Figure 33. Predicted and flight-derived open-loop unstructured stability margins of perturbed plant $\acute{G} = (I + G\Delta)^{-1}G$ for longitudinal axis at 10°, 30°, 50°, and 60° AOA.

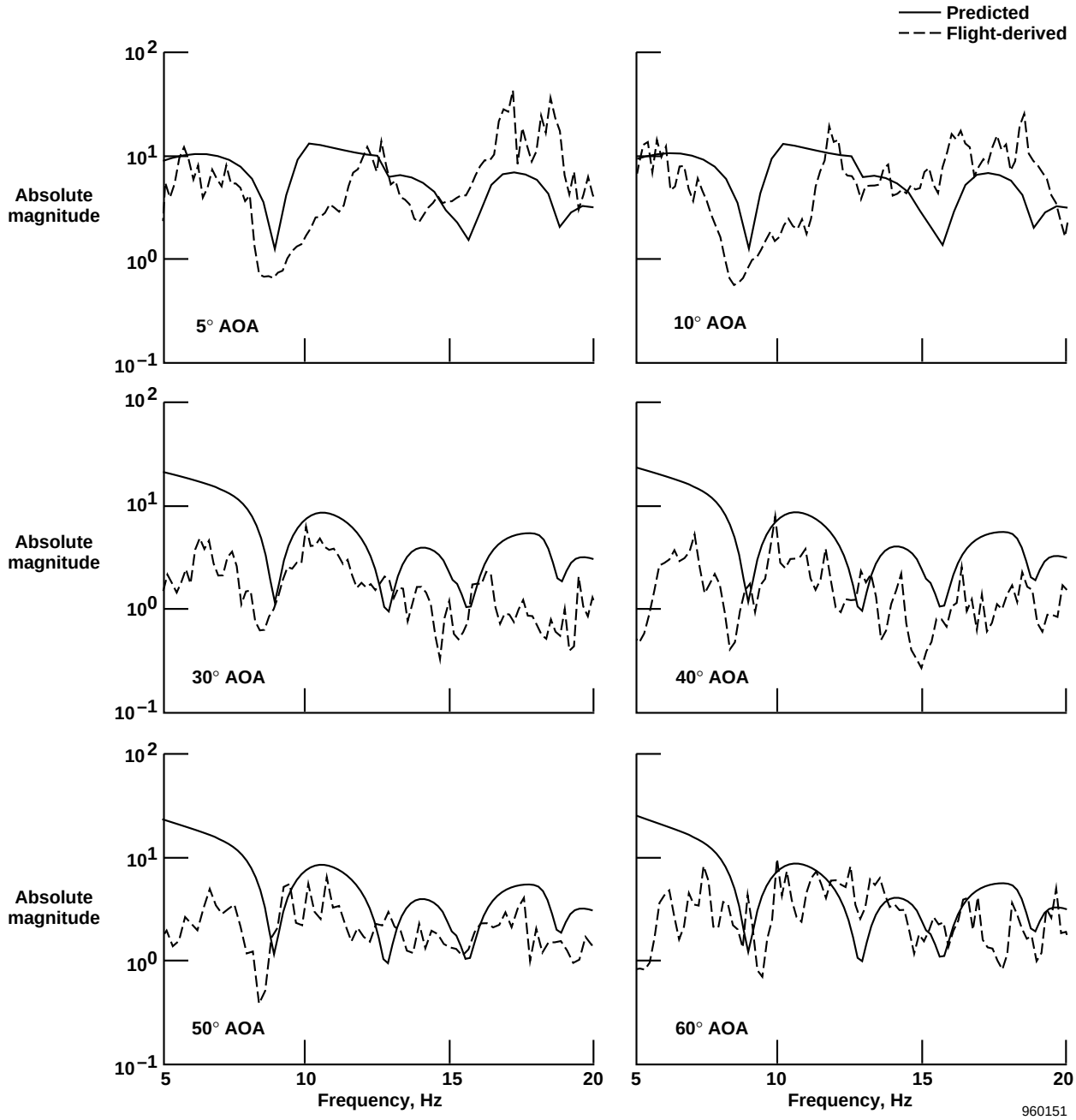

Figure 34. Predicted and flight-derived open-loop unstructured stability margins of perturbed plant $\acute{G} = (I + G\Delta)^{-1}G$ for lateral–directional axes at 5°, 10°, 30°, 40°, 50°, and 60° AOA.

Closed Loop

Above 20° AOA, the OBES input was measured to enable the generation of closed-loop results. Figure 35 shows one uncertainty description where responses are taken from surface commands to feedback with the feedback loop closed by controller *K*. As in the open-loop case, the perturbed plant $\acute{G} = (I + G\Delta)^{-1}G$ is a measure of output errors caused by input commands and disturbances. In this case, however, a different structured singular value $\mu_{\Delta}[(I - GK)^{-1}G]$ is used to compute the unstructured Δ. Figure 36 shows that differences between flight-derived and predicted perturbations to instability support the open-loop results, as would be expected if the controller dynamics were modeled properly.

Figure 37 shows a second closed-loop uncertainty interpretation to describe input sensitivity caused by input commands. The plant perturbation is represented by $\acute{G} = G(I + \Delta)^{-1}$, and $\mu_{\Delta}[(I - KG)^{-1}]$ is the multivariable stability margin used to compute Δ. In this case, however, the Δ is diagonal, or structured, because uncertainties in any input generally do not couple with another input. Figure 38 shows lateral–directional closed-loop minimum Δ plots for aileron and yaw-vectored-thrust OBES input and respective actuator command output taken after the OBES signal is summed to the actuator command signal. This multivariable stability margin result clearly indicates that, in the excited frequency range, the model again demonstrates slightly more stability robustness than the aircraft. In addition, the model and aircraft seem to agree best at the 60° AOA condition. Otherwise, discerning any specific dissimilarities is difficult because no distinguishing features exist in the data.

Finally, a third closed-loop uncertainty interpretation describes input response caused by input commands, or input complementary sensitivity (fig. 39). The perturbed plant is modeled as $\acute{G} = G(I + \Delta)$, and $\mu_{\Delta}[KG(I - KG)^{-1}]$ is the multivariable stability margin used to compute the structured Δ. Figure 40 shows lateral–directional closed-loop minimum Δ plots for the same OBES input used in figure 38, but here the output is the respective actuator commands taken before the OBES signal is summed to the actuator command signal. Beyond 15 Hz, the variance between model and aircraft is exaggerated when compared to the closed-loop plots (fig. 36), and the 60° AOA match is again clearly the best. Differences in complementary sensitivity are an indication of input errors at high frequencies, possibly because of nonlinear actuator dynamics or unmodeled high-frequency aeroelastic dynamics.

In summary, for the open-loop and two closed-loop uncertainty structures analyzed with the OBES input, the flight data and model correlate better at low AOA and very high AOA than at moderately high AOA. In other words, the region of greatest buffet activity corresponds to the largest differences between predicted and measured robust stability.

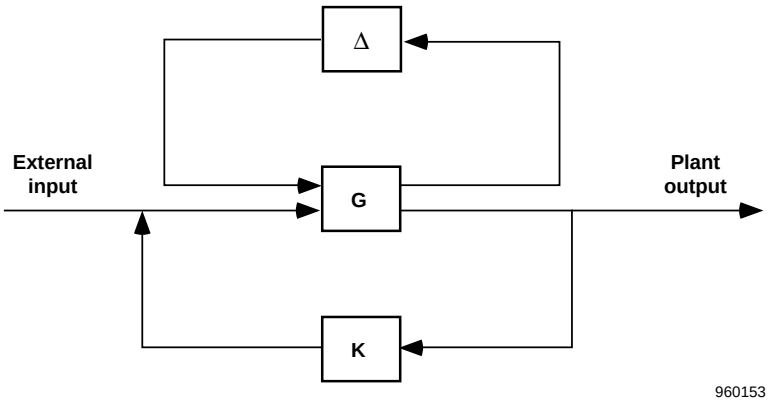

Figure 35. Closed-loop uncertainty description of output errors caused by input commands and disturbances.

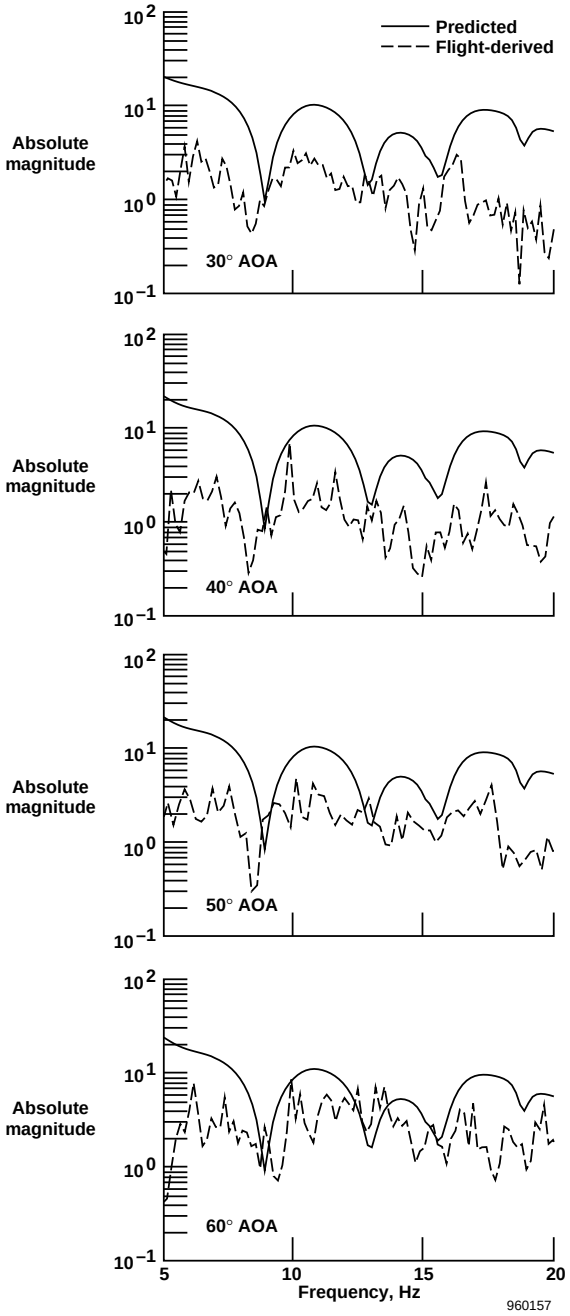

Figure 36. Predicted and flight-derived closed-loop unstructured stability margins of perturbed plant $\acute{G} = (I + G\Delta)^{-1}G$ for aileron and yaw-vectored-thrust inputs 30°, 40°, 50°, and 60° AOA.

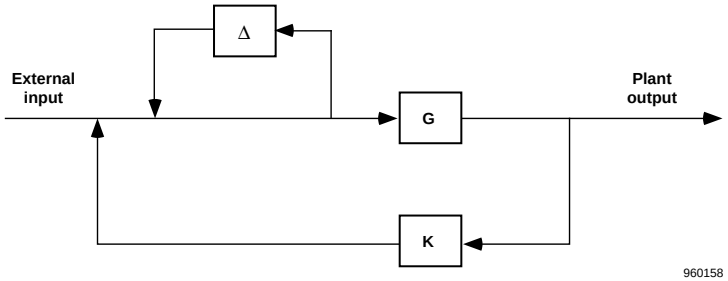

Figure 37. Closed-loop uncertainty description of input sensitivity.

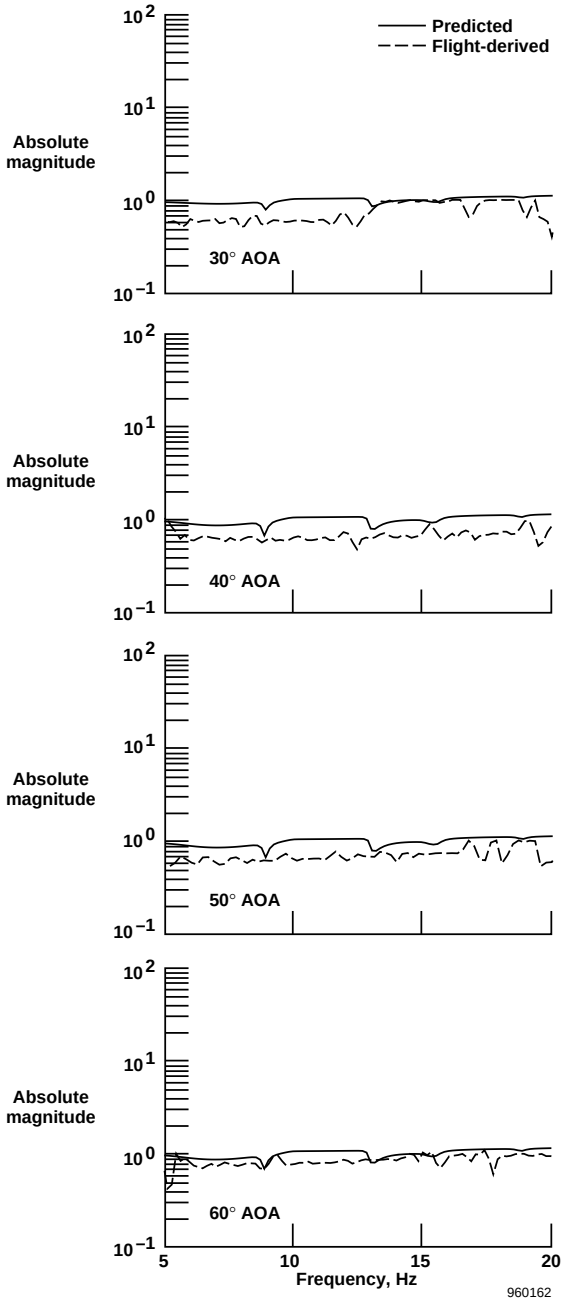

Figure 38. Predicted and flight-derived closed-loop structured stability margins of perturbed plant $\acute{G} = G(I + \Delta)^{-1}$ for aileron and yaw-vectored-thrust inputs 30°, 40°, 50°, and 60° AOA.

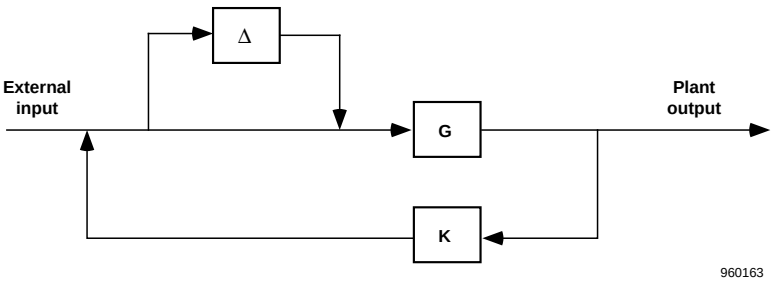

Figure 39. Closed-loop uncertainty description of input response to input commands.

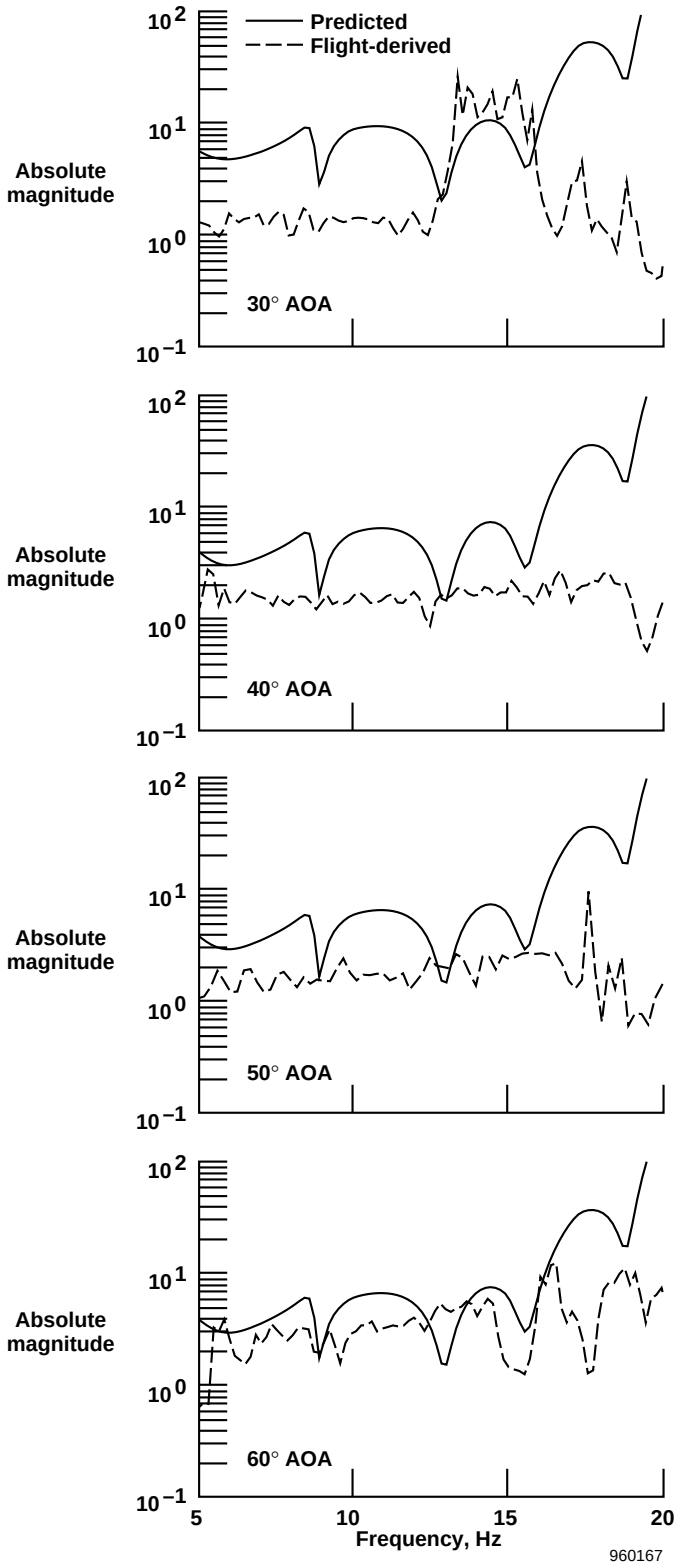

Figure 40. Predicted and flight-derived closed-loop structured stability margins of perturbed plant $\acute{G} = G(I + \Delta)$ for aileron and yaw-vectored-thrust inputs 30°, 40°, 50°, and 60° AOA.

CONCLUSIONS

Thrust vectoring at high angle of attack (AOA) adds considerable uncertainty to the standard aeroservoelastic (ASE) modeling assumptions. Efforts to refine linear unsteady aerodynamics based on potential airflow are unwarranted because this refinement does not improve the aeroelastic model accuracy. Therefore, precise servoelastic modeling for the purpose of validation with ground test results should be emphasized. Detailed actuation modeling, careful control-system augmentation, and verified feedback sensor responses are critical in properly accounting for the servoelastic coupling mechanisms. Safety of flight demands a variety of stability analyses to study the consequences of model error, and control-system augmentation depends on the type of stability analyses performed. These issues are important for any AOA, but they become more relevant for high-AOA flight at generally low dynamic pressure because of the negligible impact of modeling unsteady aerodynamic forces. At higher dynamic pressure and low AOA, the impact of unsteady aerodynamics may dominate many servoelastic dynamic coupling mechanisms, thereby reducing the criticality of these dynamics in stability and response analyses. This is evidenced by past experiences with successful ASE envelope clearance programs.

Comparisons of flight-derived and predicted modal data, transfer functions, and stability margins generally indicate good correlation. Some lateral–directional discrepancies in robust stability margins prevail throughout the buffet regime of 20° to 50° AOA, but these discrepancies are not significant. A noticeable improvement in matches between the model and flight-derived results occurs above 50° AOA. Hence, the influence of buffet acting as an unmodeled persistent disturbance is judged to be the overwhelming source of match disagreement. Regardless, servoelastic modeling and analysis retain the essential ingredients for high-AOA aeroservoelasticity.

Dryden Flight Research Center
National Aeronautics and Space Administration
Edwards, California, November 11, 1995

APPENDIX A
ACTUATOR MODELING PROCEDURE

a	servovalve port width
A_p	main ram piston area
b_l	output structural damping
b_s	attachment structural damping
C_c	$\frac{nA_p{}^2}{k_T} + \frac{V_T}{4N}$
C_f	general flow coefficient
C_p	actuator fluid flow pressure constant
C_v	main valve flow coefficient, $= C_f\, a\sqrt{\frac{P_s - P_r}{2}}$
F_e	externally applied force
G_i	ram position feedback gain to servovalve
k_l	output structural stiffness
k_s	attachment structural stiffness
k_T	combined output/attachment structural stiffness, $= \frac{1}{k_l} + \frac{1}{k_s}$
k_0, b_0, m_0	aero stiffness, aero damping, and control surface mass
k_1, b_1, m_1	modal stiffness, damping, and mass
m_p	mass of main ram piston
m_s	mass of main ram body assembly
N	bulk modulus
n	number of hydraulic systems operating
P_j	pressure difference across piston, $= P_1 - P_2$
P_r	return pressure
P_s	supply pressure
P_1	ram pressure on attachment side
P_2	ram pressure on output side
s_i	servoactuator model filter states
V_T	total fluid volume in one actuator hydraulic system
x_h	actuator ram moment arm
x_i	actuator demand from control system

x_l actuator ram displacement

x_p displacement of piston relative to main ram body, $= x_1 - x_s$

x_s actuator body displacement

x_v displacement of main control valve

x_0 displacement of control surface mass

x_1 displacement of structural modal mass

δ actual control surface rotation, $= -\frac{x_0}{x_h}$

δ_d demanded control surface rotation, $= -\frac{x_i}{x_s}$

τ_i servoactuator model filter time constants

The F/A-18 control actuation devices are redundant hydromechanical servomechanisms powered by 3000 lb/in^2 hydraulic systems. Normal hydraulic system return pressure is 85 lb/in^2, but each actuator operates at 235 lb/in^2 return pressure before dropping an additional 150 lb/in^2 at the supplied switching valves. Table A-1 lists the functional characteristics. The aileron, rudder, and turning vane actuators are operationally equivalent (they have the same ram configuration and servovalve mechanism), but they differ functionally because of dimensions. The leading-edge flap is a rotary mechanical system. The aileron actuation operation is the most popular on the aircraft because of its simplicity, so it was chosen to demonstrate the comprehensive modeling procedure.

Table A-1. F/A-18 actuation system functional characteristics.

Parameter	Vanes and ailerons	Rudder	Stabilator	Trailing-edge flap
Output force (lb)	13,100 Ext 12,090 Ret	15,740 Ext 13,880 Ret	29,940 Ext 27,250 Ret	18,070 Ext 14,330 Ret
Surface deflection (deg)	70.0	60.0	34.5	53.0
Piston area (in^2)	4.71 Ext 4.40 Ret	5.64 Ext 5.07 Ret	10.50 Ext 9.72 Ret	6.16 Ext 4.95 Ret
Stroke (in.)	4.38	1.43	7.12	8.12
Max horn arm (in.)	4.0 aileron 9.2 vane			
Output velocity (in/sec)	6.70	1.33	7.40	2.76
Surface rate (deg/sec)	100.0	56.0	40.0	18.0
Loop gain (sec^{-1})	48	37	30	18
Dynamic stiffness ($\times 10^{-5}$)	2.7 lb/in	6.0 lb/in	2.0 lb/in	0.9 lb/in
Maximum free play (deg)	0.126	0.573	0.10	0.573
Hydraulic flow (gal/min)	8.1	2.1	19.8	4.4

Methods for including detailed nonlinear actuation system models in ASE simulation analyses are cited in references 24 and 25. For a linear analysis of the actuation system, the following assumptions are made (ref. 26):

- Linear valve flow
- No valve overlaps or underlaps
- Parallel-sided valve port
- Equal fluid volumes on each side of the main ram pistons
- Equal areas on each side of the main ram pistons
- No steady load on ram
- No frictions, backlash, or hysteresis
- No limits encountered

Small-amplitude characteristics are affected by overlap, hysteresis, friction, and backlash, and large-amplitude motion is influenced by limits and port shape. This formulation does not include the effects of a dynamic leak valve (pressure feedback modulator) to reduce interaction with structural modes because it is negligible for an accurate linear analysis.

Linear modeling begins by separating elements of the actuation system into a plant, containing mechanical and hydraulic components, and a feedback system comprising servovalve and main ram feedback. Figures 10(a) and 10(b) show generic configurations of the plant and feedback elements. Servovalve dynamics are assumed to be first order combined with an inner loop position feedback. The outer loop position feedback of the relative motion between the ram piston and actuator cylinder body controls ram position according to external demand x_i from the control system. An overall actuator dynamic stiffness results from the attachment to the airframe and the lever arm attachment to the control surface. Damping comes from these attachments as well as structural mode, aerodynamic, and hydraulic origins. External force F_e may act on the main mass from a ground impedance test to check stiffness.

Flow continuity through the servovalve to force the piston is determined by flow through the valve ports, flow caused by the motion of the piston, and flow caused by fluid compressibility (bulk modulus). The derivation of linear actuation models is valid for multiple hydraulic systems using the same actuator. The systems are assumed to be identical, and the output force produced by the ram is multiplied by *n*, the number of operating systems. In matrix form, the plant equations become:

$$\begin{pmatrix} \dot{P}_j \\ \dot{x}_0 \\ \ddot{x}_0 \\ \dot{x}_1 \\ \ddot{x}_1 \end{pmatrix} = \begin{bmatrix} -b_h & 0 & -\frac{A_p}{C_1} & 0 & 0 \\ 0 & 0 & 1 & 0 & 0 \\ \frac{nA_p}{m_0} & -\frac{k_0+k_1}{m_0} & -\frac{b_0+b_1}{m_0} & \frac{k_1}{m_0} & \frac{b_1}{m_0} \\ 0 & 0 & 0 & 0 & 1 \\ 0 & \frac{k_1}{m_1} & \frac{b_1}{m_1} & -\frac{k_1}{m_1} & -\frac{b_1}{m_1} \end{bmatrix} \begin{pmatrix} P_j \\ x_0 \\ \dot{x}_0 \\ x_1 \\ \dot{x}_1 \end{pmatrix} + \begin{bmatrix} \frac{C_u}{C_1} & 0 \\ 0 & 0 \\ 0 & \frac{1}{m_0} \\ 0 & 0 \\ 0 & 0 \end{bmatrix} \begin{pmatrix} x_v \\ F_e \end{pmatrix}$$

$$\begin{pmatrix} x_p \\ x_0 \end{pmatrix} = \begin{bmatrix} \frac{nA_p}{k_T} & 1 & 0 & 0 & 0 \\ 0 & 1 & 0 & 0 & 0 \end{bmatrix} \begin{pmatrix} P_j \\ x_0 \\ \dot{x}_0 \\ x_1 \\ \dot{x}_1 \end{pmatrix} + \begin{bmatrix} 0 & 0 \\ 0 & 0 \end{bmatrix} \begin{pmatrix} x_v \\ F_e \end{pmatrix}$$

The sign convention assumes that actuator extension always gives negative hinge moment and control rotation. By augmenting this plant description with the servovalve and ram feedback (fig. 10(b)), the F/A-18 aileron actuator equations become the following (where *X* denotes a nonzero value):

$$\begin{pmatrix} \dot{s}_2 \\ \dot{s}_1 \\ \dot{s}_0 \\ \dot{P}_j \\ \dot{x}_0 \\ \ddot{x}_0 \\ \dot{x}_1 \\ \ddot{x}_1 \\ \dot{s}_3 \end{pmatrix} = \begin{bmatrix} -\frac{1}{\tau_2} & 0 & 0 & 0 & 0 & 0 & 0 & 0 & X \\ X & -\frac{1}{\tau_1} & X & 0 & 0 & 0 & 0 & 0 & 0 \\ 0 & 1 & 0 & 0 & 0 & 0 & 0 & 0 & 0 \\ 0 & 0 & X & -b_h & 0 & -\frac{A_p}{C_1} & 0 & 0 & 0 \\ 0 & 0 & 0 & 0 & 0 & 1 & 0 & 0 & 0 \\ 0 & 0 & 0 & \frac{nA_p}{m_0} & -\frac{k_0+k_1}{m_0} & -\frac{b_0+b_1}{m_0} & \frac{k_1}{m_0} & \frac{b_1}{m_0} & 0 \\ 0 & 0 & 0 & 0 & 0 & 0 & 0 & 1 & 0 \\ 0 & 0 & 0 & 0 & \frac{k_1}{m_1} & \frac{b_1}{m_1} & -\frac{k_1}{m_1} & -\frac{b_1}{m_1} & 0 \\ 0 & 0 & 0 & X & X & 0 & 0 & 0 & -\frac{1}{\tau_3} \end{bmatrix} \begin{pmatrix} s_2 \\ s_1 \\ s_0 \\ P_j \\ x_0 \\ \dot{x}_0 \\ x_1 \\ \dot{x}_1 \\ s_3 \end{pmatrix} + \begin{bmatrix} -x_h G_i \\ 0 \\ 0 \\ 0 \\ 0 \\ 0 \\ 0 \\ 0 \\ 0 \end{bmatrix} \delta_d$$

$$\begin{pmatrix} \delta \\ \dot{\delta} \\ x_p \end{pmatrix} = \begin{bmatrix} 0 & 0 & 0 & 0 & -\frac{1}{x_h} & 0 & 0 & 0 & 0 \\ 0 & 0 & 0 & 0 & 0 & -\frac{1}{x_h} & 0 & 0 & 0 \\ 0 & 0 & 0 & \frac{nA_p}{k_T} & 1 & 0 & 0 & 0 & \end{bmatrix} \begin{pmatrix} s_2 \\ s_1 \\ s_0 \\ P_j \\ x_0 \\ \dot{x}_0 \\ x_1 \\ \dot{x}_1 \\ s_3 \end{pmatrix}$$

Given the extensive assumptions for linearity and ignoring other system components such as a dynamic leak valve, damper accumulator, or some other pressure feedback modulation, the model is not expected to match measured results exactly. A model for friction would generally add some damping. In addition, the fluid coefficients C_p, C_v, and C_f are susceptible to error, and the fluid bulk modulus *N* may differ depending on the type of operating system (ref. 27). These parameters may be tuned to match test data. For the F/A-18 actuators, the servovalve port width *a* (or equivalently, the main valve flow coefficient C_v) and fluid flow pressure constant C_p required adjustment to account for variations in valve port shape and size.

APPENDIX B
CONTROLS AUGMENTATION

Discretization and Time Delays

The ASE model realization differs according to the desired goals. References 28 and 29 explain how to model hybrid continuous and discrete systems subject to arbitrary delays and multiple (possibly asynchronous) sample rates for frequency response analyses. Time response and eigenvalue analyses are performed by discretizing the plant at the highest loop sample rate, $1/T$, using the method of zero-order hold (ZOH) equivalence (matrix exponential), and the method described in reference 30 to incorporate control processor time delay $\tau = mT - \lambda$, where T is the sample time, m is an integer, and λ is a fractional delay difference (assuming $m \geq 0$ and $0 \leq \lambda < T$). Treatment of the case $m = 0, \tau = -\lambda$ is actually prediction and will not be discussed. Here, we consider only the case $m = 1, \lambda \neq 0$. First, define

$$\Phi = e^{\bar{A}T}, \quad \Gamma_1 = \int_{\lambda}^{T} e^{\bar{A}t}\bar{B}\ dt, \Gamma_2 = \int_{0}^{\lambda} e^{\bar{A}t}\bar{B}\ dt$$

For any positive scalar a define

$$\Phi(a) = e^{\bar{A}a}, \quad \Psi(a) = \frac{1}{a}\int_{0}^{a} e^{\bar{A}t}dt$$

Next write

$$\Gamma_1 = \Phi(\lambda)\Psi(T-\lambda)(T-\lambda)\bar{B}$$

$$\Gamma_2 = \Psi(\lambda)\lambda\bar{B}$$

Only the exponential series for Ψ need be computed because it can be shown that

$$\Phi(a) = I + \Psi(a)a\bar{A}$$

The state equations are now given by

$$x(k+1) = \Phi x(k) + \Gamma_1 u(k-1) + \Gamma_2 u(k)$$

Define the new state $x_{n+1}(k) = u(k-1)$ to form the new system

$$\begin{pmatrix} x(k+1) \\ x_{n+1}(k+1) \end{pmatrix} = \begin{bmatrix} \Phi & \Gamma_1 \\ 0 & 0 \end{bmatrix}\begin{pmatrix} x(k) \\ x_{n+1}(k) \end{pmatrix} + \begin{bmatrix} \Gamma_2 \\ I \end{bmatrix}u(k)$$

$$y = \begin{bmatrix} \bar{C} & 0 \end{bmatrix}\begin{pmatrix} x \\ x_{n+1} \end{pmatrix} + \bar{D}u(k)$$

The formulation now adds delayed control input to the state vector for delay times less than the smallest loop sample time, appears computationally attractive, and requires no approximation (as opposed to the common technique

which uses low-order Padé approximates for delays). This plant description is used for computation of time responses and open-loop eigenvalues.

ZOH and time delays are treated differently in frequency response analyses. Plant dynamics are Laplace transformed and augmented with analog elements, including sensors and prefilters, using standard procedures. Then, the continuous system with time delay τ is formulated as

$$y(s) = \left(\frac{H(s)[ZOH]}{T}\right)u(s)$$
$$= H^*(s, \tau, T)u(s)$$

where

s = Laplace variable

$H(s) = \left[\bar{C}(sI - \bar{A})^{-1}\ \bar{B} + D\right]$

$[ZOH]$ = is the zero-order hold complex expression $\left(= e^{-s\tau}\ \frac{1 - e^{-sT}}{s}\right)$

and where $H^*(s, \tau, T)$ is now the plant transfer function for all continuous dynamics.

Digital Filter Realization

Because digital filter realizations are critical to the validity of the model, the implementation of discrete filters in the flight computer hardware is considered more important than the problem of approximating the action of an analog element on a continuous waveform with a linear digital filter operating on a sampled continuous waveform. The former realization can differ significantly from the latter, which is the correct duplication of elements such as sensors and prefilters. Consequently, if the computer software uses the standard *z* transform discretization, this realization should be used in the analysis. Alternatively, because the *z* transform suffers drawbacks caused by power aliasing about the Nyquist frequency and the implementation of high-pass filters, another discretization should be used for the analog elements if the objective is time response or eigenvalue checks. A technique that performs extremely well in flight simulations is based on the bilinear transformation but gives the same pole and zero locations as the matched *z* transform algorithm, with additional zeros added at $z = -1$ for all *s*-plane zeros at infinity. Given the continuous transfer function $G_s(s)$, the poles and zeros contained in the primary strip of the *s*-plane are mapped into the left half of the intermediate *w*-plane with the complex transformation

$$w = \tanh\frac{sT}{2}$$

This maps a root located at $s = \sigma + i\varepsilon$ to the *w*-plane root $w = \mu + i\eta$, where

$$\mu = \frac{\sinh\sigma T}{\cosh\sigma T + \cos\varepsilon T}, \quad \eta = \frac{\sin\varepsilon T}{\cosh\sigma T + \cos\varepsilon T}$$

The intermediate result $G_w(w)$ is a mapping of the *s*-plane imaginary axis from $-(\pi/T)$ to π/T onto the entire imaginary axis of the *w*-plane from $-\infty$ to ∞. The *s*-plane negative real axis maps onto the *w*-plane negative real axis from 0 to –1. Now the function $G_w(w)$ is mapped into the unit circle of the *z*-plane with

$$z = \frac{1+w}{1-w}$$

to the *z*-plane location

$$Re(z) = \frac{1-\mu^2+\eta^2}{(1-\mu)^2+\eta^2}, \quad Im(z) = \frac{2\eta}{(1-\mu)^2+\eta^2}$$

This results in a mapping from *s*-plane to *z*-plane where the poles and zeros are related by $z = e^{sT}$ and infinite *s*-plane zeros are mapped to $z = -1$. Computationally, the complete algorithm is stated as transforming the continuous $G_s(s)$ given by

$$G_s(s) = \frac{K_s \Pi_{i=1}^{u}(s+\alpha_i)\Pi_{i=1}^{n}\left[(s+\alpha_i)^2+b_i^2\right]}{\Pi_{i=1}^{r}(s+\beta_i)\Pi_{i=1}^{t}\left[(s+c_i)^2+d_i^2\right]}$$

to the digital filter

$$G_z(z) = \frac{K_z(z+1)^k \Pi_{i=1}^{u}\left(z-e^{-\alpha_i T}\right)\Pi_{i=1}^{n}\left[\left(z^2-2e^{-a_i T}\cos b_i T z+e^{-2a_i T}\right)\right]}{\Pi_{i=1}^{r}\left(z-e^{-\beta_i T}\right)\Pi_{i=1}^{t}\left[\left(z^2-2e^{-c_i T}\cos d_i T z+e^{-2c_i T}\right)\right]}$$

where $k = r+2t-u-2n, k \geq 0$, and K_z is the normalization constant such that for unity gain low-pass filters, $G_z(z=1) = 1$ and for high-pass filters, $G_z(z=-1) = 1$. Integral time delays are represented by the *n* unit delays $z^{-n}G_z(z)$. This algorithm, similar to matched pole-zero mapping, gives good time response accuracy with its continuous equivalent. It cannot be used for multi-input–multi-output (MIMO) transfer functions, so each single-input–single-output (SISO) analog element is treated separately. A practical consideration for numerical accuracy when augmenting these transfer functions is to limit the denominator order to second or third so the range of coefficient magnitudes is kept reasonable in the numerator and denominator.

Multirate Representation

Feedback for the F/A-18 basic and RFCS control laws, longitudinal and lateral–directional, is a mixture of 80-Hz and 40-Hz sampling rates. Figure 14(a) shows a simple schematic of the procedure for modeling hybrid multirate systems for frequency response analyses. In this model, the feedback is sampled at $1/T_3$ and $1/T_4$, the reference and error signals are sampled at $1/T$, and control surfaces are commanded at $1/T_1$ and $1/T_2$, designated in the ZOH. The $1/T$ factor in the ZOH is derived by taking the limit of a sampled spectrum as the sample time goes to zero, thereby resulting in the continuous spectrum of the discretely excited plant. Aircraft dynamics are described by Laplace transformed state equations, so system transfer functions are all well-defined functions of the Laplace variable *s* similar to the single-rate hybrid formulation.

In the RFCS control laws, where sample time $T = 0.0125$, slower rate 40-Hz feedback is converted to faster 80-Hz signals using discrete memory averagers $M(z) = \frac{1+z}{2z}$, where $z = e^{sT}$. The multirate character of feedback is disguised, and all digital filters $G_i(z)$ can be implemented as 80-Hz discretizations. Averagers are generally represented by

$$M(z) = \frac{\sum_{k=0}^{n-1} z^k}{nz^{n-1}}$$

where the rate ratio $n = T_i/T$ is an integer. Discrete memory $M(z)$ is also used for stability and time response analysis of multirate systems. Figure 14 shows two different multirate implementations for eigenvalue analyses. In figure 14(b), plant dynamics are discretized at the fastest rate $1/T$ using zero-order hold equivalence and slower feedback are passed through the appropriate $M(z)$. Any filters $G_i(z)$ calculated and implemented for slower rate signals substitute $z = e^{sT_i}$. Slow rate control commands are also averaged before being passed to the actuator. Alternatively, in figure 14(c), plant dynamics are discretized at the slowest rate and any internal fast rate loops and fast control commands are augmented with $M^{-1}(z)$, the inverse of $M(z)$. The substitution of $z = e^{sT_i}$ in the fast filters follows accordingly. In the case of the RFCS control laws, the fast controller formulation matched the measured ground test results more closely than the slow rate formulation did.

REFERENCES

1. Gupta, K.K., M.J. Brenner, and L.S. Voelker, *Development of an Integrated Aeroservoelastic Analysis Program and Correlation with Test Data*, NASA TP-3120, May 1991.

2. Zislin, A., E. Laurie, K. Wilkinson, and R. Goldstein, "X-29 Aeroservoelastic Analysis and Ground Test Validation Procedures," AIAA 85-3091, AIAA/AHS/ASEE Aircraft Design Systems and Operations Meeting, Colorado Springs, Colorado, Oct. 1985.

3. Cheng, Peter Y., R.C. Jones, and S.M. Murnyack, "STOL Maneuver Technology Demonstrator Aeroservoelasticity," AIAA Guidance, Navigation, and Control Conference, Portland, Oregon, Aug. 1990.

4. Pahle, Joseph W., Bruce Powers, Victoria Regenie, Vince Chacon, Steve Degroote, and Steven Murnyack, *Research Flight Control System Development for the F-18 High-Alpha Research Vehicle*, NASA TM-104232, 1991.

5. Gilbert, W.P., L.T. Nguyen, and J. Gera, "Control Law Research in the NASA High Alpha Technology Program," AGARD CP-465, Apr. 1991.

6. Gupta, K.K., *STARS - An Integrated General-Purpose Finite Element Structural, Aeroelastic, and Aeroservoelastic Analysis Computer Program*, NASA TM-101709, 1990.

7. Taylor, R.F., K.L. Miller, and R.A. Brockman, *A Procedure for Flutter Analysis of FASTOP-3 Compatible Mathematical Models, Volume 1 - Theory and Application*, AFWAL-TR81-3063.

8. Tiffany, H. Sherwood, and William M. Adams, Jr., *Nonlinear Programming Extensions to Rational Function Approximation Methods for Unsteady Aerodynamic Forces*, NASA TP-2776, Jul. 1988.

9. Bublitz, P. and H. Zingel, "Experimental Investigations of Buffet Excitation Forces on a Low Aspect Ratio Trapezoidal Half Wing in Incompressible Flow," *Aircraft Dynamic Loads due to Flow Separation*, AGARD CP-483, 1990.

10. Forsching, H.W., "Unsteady Aerodynamic Forces on an Oscillating Wing at High Incidences and Flow Separation," *Aircraft Dynamic Loads due to Flow Separation*, AGARD CP-483, 1990.

11. Bowers, Albion H., Gregory K. Noffz, Sue B. Grafton, Mary L. Mason, and Lee R. Peron, *Multiaxis Thrust Vectoring Using Axisymmetric Nozzles and Postexit Vanes on an F/A-18 Configuration Vehicle*, NASA TM-101741, Apr. 1991.

12. Zimmerman, Helmut, "Aeroservoelasticity," *Computer Methods in Applied Mechanics and Engineering*, vol. 90, pp. 719–735, 1991.

13. Brenner, Martin J., "Actuator and Aerodynamic Modeling for High-Angle-of-Attack Aeroservoelasticity," AIAA 93-1419, Apr. 1993.

14. Waszak, Martin R. and David K. Schmidt, "On the Flight Dynamics of Aeroservoelastic Vehicles," AIAA 86-2077.

15. Chan, Samuel Y., et. al., *Aeroservoelastic Stabilization Techniques for Hypersonic Flight Vehicles*, NASA CR-187614, Sept. 1991.

16. Doyle, John, "Analysis of Feedback Systems with Structured Uncertainties," *IEEE Proceedings*, vol. 129, part D, no. 6, Nov. 1982.

17. Enns, Dale F., "Development of Control Law Methodology for the Oblique Wing Research Aircraft," Final Report, Honeywell ADG Report F0202-SR1, Jun. 1986.

18. Enns, Dale F., Joe E. Wall, Russ C. Hendrick, and Steven D. Ginter, *Analysis of the Flight Control Laws for the Forward Swept Wing Aircraft*, NASA CR-166621, Oct. 1986.

19. Cole, Stanley R., Steven W. Moss, and Robert V. Doggett, Jr., *Some Buffet Response Characteristics of a Twin-Vertical-Tail Configuration*, NASA TM-102749, 1990.

20. Lee, B.H.K., D. Brown, M. Zgela, and D. Poirel, "Wind Tunnel Investigation and Flight Tests of Tail Buffet on the CF-18 Aircraft," AGARD CP-483, 1990.

21. Ferman, M.A., S.R. Patel, N.H. Zimmerman, and G. Gesternkorn, "A Unified Approach to Buffet Response of Fighter Aircraft Empennage," AGARD CP-483, 1990.

22. Balas, Gary J., John C. Doyle, Keith Glover, Andy Packard, and Roy Smith, μ *-Analysis and Synthesis Toolbox*, MUSYN Inc., and The MathWorks, Inc., Apr. 1991.

23. Doyle, John C., Joseph E. Wall, and Gunter Stein, "Performance and Robustness Analysis for Structured Uncertainty," Proceedings of the 20th IEEE Conference on Decision and Control, Orlando, Florida, 1982.

24. Stirling, R., "Flexible Aircraft and Control System Dynamics," University of Bristol, Dept. of Aeronautical Engineering report no. RS/3/84, Jul. 1984.

25. Stirling, R. and D.A. Cowling, "Implementation of Comprehensive Actuation System Models in Aeroservoelastic Analysis," Presented at the *European Forum on Aeroservoelasticity and Structural Dynamics*, Aachen, Germany, report no. SDL 143, Apr. 1989.

26. Stirling, R., "Linearized Model of the Jaguar Fly-by-Wire Actuation System," University of Bristol, Dept. of Aeronautical Engineering report no. RS/2/83, Oct. 1983.

27. Edwards, John W., *Analysis of an Electrohydraulic Aircraft Control-Surface Servo and Comparisons with Test Results*, NASA TN D-6928, Aug. 1972.

28. Whitbeck, R.F. and L.G. Hofmann, "Analysis of Digital Flight Control Systems with Flying Qualities Applications," AFFDL-TR-78-115.

29. Whitbeck, R.F., D.G.L. Didaleusky, and L.G. Hofmann, "Frequency Response of Digitally Controlled Systems," AIAA 81-4169.

30. Franklin, Gene F. and J. David Powell, *Digital Control of Dynamic Systems*, Addison-Wesley Publishing Co., Philippines, 1980.

REPORT DOCUMENTATION PAGE

Form Approved
OMB No. 0704-0188

1. AGENCY USE ONLY (Leave blank)	2. REPORT DATE	3. REPORT TYPE AND DATES COVERED
	September 1996	Technical Paper

4. TITLE AND SUBTITLE

Aeroservoelastic Modeling and Validation of a Thrust-Vectoring F/A-18 Aircraft

5. FUNDING NUMBERS

WU 505-68-30

6. AUTHOR(S)

Martin J. Brenner

7. PERFORMING ORGANIZATION NAME(S) AND ADDRESS(ES)

NASA Dryden Flight Research Center
P.O. Box 273
Edwards, California 93523-0273

8. PERFORMING ORGANIZATION REPORT NUMBER

H-2081

9. SPONSORING/MONOTORING AGENCY NAME(S) AND ADDRESS(ES)

National Aeronautics and Space Administration
Washington, DC 20546-0001

10. SPONSORING/MONITORING AGENCY REPORT NUMBER

NASA TP-3647

11. SUPPLEMENTARY NOTES

12a. DISTRIBUTION/AVAILABILITY STATEMENT

Unclassified—Unlimited
Subject Category 08

12b. DISTRIBUTION CODE

13. ABSTRACT (Maximum 200 words)

An F/A-18 aircraft was modified to perform flight research at high angles of attack (AOA) using thrust vectoring and advanced control law concepts for agility and performance enhancement and to provide a testbed for the computational fluid dynamics community. Aeroservoelastic (ASE) characteristics had changed considerably from the baseline F/A-18 aircraft because of structural and flight control system amendments, so analyses and flight tests were performed to verify structural stability at high AOA. Detailed actuator models that consider the physical, electrical, and mechanical elements of actuation and its installation on the airframe were employed in the analysis to accurately model the coupled dynamics of the airframe, actuators, and control surfaces. This report describes the ASE modeling procedure, ground test validation, flight test clearance, and test data analysis for the reconfigured F/A-18 aircraft. Multivariable ASE stability margins are calculated from flight data and compared to analytical margins. Because this thrust-vectoring configuration uses exhaust vanes to vector the thrust, the modeling issues are nearly identical for modern multiaxis nozzle configurations. This report correlates analysis results with flight test data and makes observations concerning the application of the linear predictions to thrust-vectoring and high-AOA flight.

14. SUBJECT TERMS

Aeroservoelasticity, Aircraft vibration, Dynamic stability, F/A-18 aircraft, Flight dynamics, Structural dynamics, Thrust vectoring

15. NUMBER OF PAGES

65

16. PRICE CODE

A03

17. SECURITY CLASSIFICATION OF REPORT	18. SECURITY CLASSIFICATION OF THIS PAGE	19. SECURITY CLASSIFICATION OF ABSTRACT	20. LIMITATION OF ABSTRACT
Unclassified	Unclassified	Unclassified	Unlimited

NSN 7540-01-280-5500

Available from the NASA Center for AeroSpace Information, 800 Elkridge Landing Road, Linthicum Heights, MD 21090; (301)621-0390

Standard Form 298 (Rev. 2-89)
Prescribed by ANSI Std. Z39-18
298-102